Effect of thickness-to-chord ratio on the wake of two-dimensional rectangular cylinders

Meraj Mohebi, Phillip du Plessix, Robert J. Martinuzzi,* and David H. Wood
Department of Mechanical and Manufacturing Engineering, University of Calgary, Calgary, Alberta T2N 1N4, Canada
(Received 15 November 2016; published 26 June 2017)

The dynamics of the nearly periodic highly modulated turbulent wakes of two-dimensional rectangular cylinders normal to a uniform flow are investigated experimentally for thickness-to-chord ratios between 0.05 and 1.92 at Reynolds numbers around 6 600. Measurements were conducted using planar, time-resolved stereoscopic particle image velocimetry. A generalized phase average analysis, which invokes elements of mean-field theory to relate the temporal modal coefficients of the fundamental harmonic and slow-varying base-flow drift, provided a statistically significant representation of the coherent cycle-to-cycle variation of the shedding process. It is shown that the characteristics of the wake velocity fluctuations change as a function of the thickness-to-chord ratio and can be related to structural differences in the wake topology. Moreover, the trajectory of shed vortices plays an important role in distinguishing the dynamics observed for different fluctuation-amplitude cycles. Based on differences in amplitude modulation characteristics and the vortex formation region topology, three flow regimes can be defined: a thin-plate regime, for which the feedback between forming vortices and base pressure is important; a cylinder-like thick-plate regime for which the obstacle afterbody suppresses the feedback; and a long-plate regime for which wake periodicity is not associated with the classical Kármán shedding process. The present analysis highlights the importance of the feedback mechanism for the thin-plate regime and helps reconcile differences in the reported critical thickness values between regimes.

DOI: 10.1103/PhysRevFluids.2.064702

I. INTRODUCTION

The turbulent wake of a two-dimensional (2D) rectangular cylinder[1] normal to the flow is a fundamental yet complicated aerodynamics problem relevant to many engineering applications such as tall structures, buildings, and long-span bridges exposed to wind. The forces caused by vortex shedding can excite damaging frequencies of flexible structures. Investigating the physical processes underlying the vortex shedding characteristics allows design optimization and flow control. In order to understand both the mean and unsteady forces for engineering applications, simplified bluff body models such as 2D circular, rectangular, and H- and D-shaped cylinders have been the subject of substantial research in the past. The wakes of these bluff bodies are also of interest in heat and mass transfer research [1] as turbulence can affect the heat transfer rate, in applications such as stays and supports in internal flow geometries as found in heat exchangers, or erosion rates behind piers.

Fage and Johansen [2], using hot-wire anemometry and surface pressure measurements for a 2D plate of thickness (b, streamwise thickness when the plate is held normal to the flow) to width (d, the width or chord) ratio of 0.03, were among the first to characterize the wake periodicity for rectangular geometries and reported shedding frequencies, f_{sh}, in terms of the nondimensional

*Corresponding author: rmartinu@ucalgary.ca

[1]Strictly, these "cylinders" are sharp-edged prisms, but are called "cylinders" in the vast majority of the literature. In conformity to the literature, we will refer to a cylinder with small thickness-to-width ratios, typically less than 0.2, as a "plate."

Strouhal number $St = f_{sh}d/U_\infty$ (U_∞ being the uniform free-stream velocity). The literature on normal rectangular cylinders is mostly focused on the thin flat plate, b/d typically less than 0.2 [2–7], and the square cylinder, $b/d = 1.0$ [8–13]. Intermediate thickness ratios have received much less attention and the effect of b/d on the flow is not fully understood, but small variations in b/d can affect the drag coefficient [14] ($C_d = \text{Drag}/\frac{1}{2}\rho U_\infty^2 d$, $\rho =$ fluid density). Surface pressure coefficient [$C_p = (P - P_\infty)/\frac{1}{2}\rho U_\infty^2$, P is the local pressure, P_∞ is the free-stream pressure], C_d, and St data for normal rectangular cylinders as a function of b/d have been measured in several studies [15–23]. Some of the experiments were for forced oscillation shedding [24–26] whose resemblance to natural shedding is not obvious. However, Nakamura and Ohya [27], among others, found that as b/d is increased from nominally zero, there are multiple parameters that can affect the flow and make a comparison troublesome. These experimental parameters include the tunnel blockage (B, the ratio of the obstacle to the test section frontal areas), free-stream turbulence intensity (Tu, defined in the conventional manner as the root-mean-square of the streamwise fluctuations divided by U_∞), end conditions, aspect ratio (AR, ratio of the span s to d of a rectangular cylinder), and Reynolds number ($Re = \rho U_\infty d/\mu$, $\mu =$ dynamic viscosity of the fluid).

A synthesis of the available literature suggests some consensus for $b/d \lesssim 1.7$–2. The flow separates at the sharp leading edges and, in the mean, does not reattach on the "afterbody" (i.e., body surfaces downstream of the separation points). The wake periodicity is due to a Kármán-like process of vortex formation and shedding. Generally, the influence of the turbulence intensity is negligible for Tu $\lesssim 3\%$ and the flow is relatively insensitive to the Reynolds number for $Re > 4\,000$.

The drag coefficient C_d has been reported [14] to increase as the thickness ratio was increased from $b/d = 0.2$, reaching a peak value at a critical thickness of 0.6 and decreased monotonically as b/d was further increased to $b/d \approx 2$. The frequency of vortex shedding, in terms of St, decreased from $b/d = 0.2$ to $b/d = 0.6$ and was nearly constant as b/d was further increased to $b/d \approx 1.5$ and decreased for larger b/d. Qualitatively similar results were found in later studies. While similar values of the critical thickness for maximum C_d have been reported [16,23,28], differences reported by Igarashi [22] and Knisely [29] indicate that the aspect ratio, and thus the end conditions, influence the value of the critical thickness. However, differences in the reported values of the critical thickness as obtained from different large-eddy simulation (LES) studies [30–32], ranging from ~ 0.4 to 0.6, suggest more subtle effects as well.

A significant scatter in both the values and trends is observed when comparing results of St as a function of b/d from different studies. References [16,24,28,29,33,34] report similar trends for St as a function of b/d as reported in Ref. [14], but their values for St are noticeably higher than in the latter study. In contrast, Refs. [35] and [22] suggest an increase in St as b/d is increased to the critical thickness, while Ref. [23] shows little change in St. As b/d is further increased, these studies report a monotonic decrease in St up to $b/d \sim 1.7$–2. Despite the difference in trends reported for St as a function of b/d, all results indicate a change at or close to the point of maximum C_d. Several LES studies [30–32,36] report that for obstacles with b/d less than the critical thickness, the fluctuation amplitude for the base pressure, lift, and drag coefficients are significantly more modulated than for thicker obstacles. This change has been attributed to a change in the vortex formation process in the base region. At the critical thickness that maximized C_d, Ref. [28] observed that the base pressure coefficient C_{pb} has alternating low and high values at irregular intervals. Based on visualizations [28,37], albeit at a much lower $Re < 4\,000$, these changes were associated with an abrupt change between two different flow patterns. It remains, however, that evidence is restricted to low-Re visualizations and the nature of the changes is still not elucidated.

A second critical thickness was found between $b/d \approx 1.7$ and 3 [21,23,29,31,32,38,39] for which the flow separating from the leading edge reattaches to the afterbody. While periodicity in the wake velocity fluctuations is observed, it is unclear whether the vortex formation process corresponds to the more conventional Kármán-like process observed for thinner cylinders. The state of the developing boundary layer near the trailing edge of the obstacle plays an important role in determining the flow characteristics. The state is very sensitive to Tu and Re, e.g., see Refs. [21] or [39], explaining the

large scatter in the reported values for St, C_d, and the value of this second critical thickness for such elongated cylinders.

The nature of the changes in the vortex shedding at different thickness ratios has not been experimentally characterized in terms of vortex topology and strength during the formation and shedding process. Such a characterization requires spatially correlated measurements over the shedding cycle. To the authors' knowledge, almost all previous studies are limited to hot-wire anemometry, surface pressure measurements, force balances, and smoke-dye visualizations. These methods mainly provide information on St, C_d, surface pressure evolution, and a limited number of velocity profiles. Because of the inherent limitation of hot-wire anemometry, these velocity profiles are obtained significantly downstream of the formation region such that even conditionally averaged measurements do not provide insight into changes in the formation and shedding process.

It is noted that Refs. [6] and [12] report conditionally ensemble-average velocity fields according to the shedding phase for a thin plate ($b/d = 0.08$) and a square cylinder ($b/d = 1$), respectively.

This traditional phase average (TPA) provides a representation of an average shedding cycle. The results for the square cylinder include the base formation region and show a high level of coherence with the shedding motion, whereby it is reported that up to 60% of the total Reynolds stress contributions are due to the coherent motion. Unfortunately, for the thin plate case, only the region downstream of the formation region is presented, showing a formed vortex street. Leder [6] observed coherent contributions to the Reynolds stress field that are significantly lower than for the square cylinder. Ohya [28] and others have shown that the amplitude modulation of the periodic fluctuations in the leeward face pressure and wake velocity fluctuations is significantly higher for thinner plates. Moreover, the modulation and variation levels depend on the thickness ratio, suggesting that an average cycle TPA representation may mask some important flow dynamics.

In the present work, coherent cycle-to-cycle variations in the vortex shedding characteristics, wake topology, and dynamics are captured from stereoscopic particle image velocimetry (stereo-PIV) measurements using a generalized phase averaging (GPA) technique [40]. Here, the three most energetic proper orthogonal decomposition (POD) modes are related via mean-field theory of Ref. [41] in phase space to construct the GPA model for the coherent contribution to the cycle-to-cycle variations.

This paper presents stereo-PIV measurements of all mean velocities, Reynolds stresses, and triple products in the wake of 2D rectangular cylinders normal to a wind tunnel flow. The b/d ratios were varied between 0.05 and 1.92 at $Re \approx 6\,600$, with AR ≈ 38. The effect of b/d on the wake structure and the vorticity field is described in the form of mean flow, turbulent statistics, shedding frequencies, and unsteady vortex shedding process. The drag coefficient was found from the mean momentum equations applied at the end of field of view. The remainder of the paper is laid out as follows. Section II describes the experimental facility and details of the stereo-PIV acquisition. The principals and the implementation methodology of the GPA technique are summarized in Sec. III A. Subsequently, an overview of the mean field is given in Sec. IV A and observations on the nature of the vortex shedding based on the GPA are presented and discussed in Sec. IV B. Key observations from the analysis are discussed and related to findings in the earlier literature in Sec. V. The final section provides the main conclusions.

II. EXPERIMENTAL FACILITY

The experimental setup is shown schematically in Fig. 1 together with the nomenclature. Measurements were performed in an open jet working section wind tunnel. Still air is drawn through a 3-m-diameter inlet and passes through three 20-mesh metal grids, a 24- and 30-mesh metal grid, and one 80-mesh nylon screen into a contraction section of area ratio 36:1. The working section of the wind tunnel is a 0.5-m-diameter jet in which the experimental apparatus was mounted. The working section free-stream velocity is $U_\infty = 8.70 \pm 0.05$ m/s and was monitored with a Pitot-static tube. The free-stream turbulence intensity ($\sqrt{\overline{u'^2}}/U_\infty$) is 0.8%. The ambient temperature and pressure were constant throughout the measurements nominally at 20°C and 90 kPa(a), respectively.

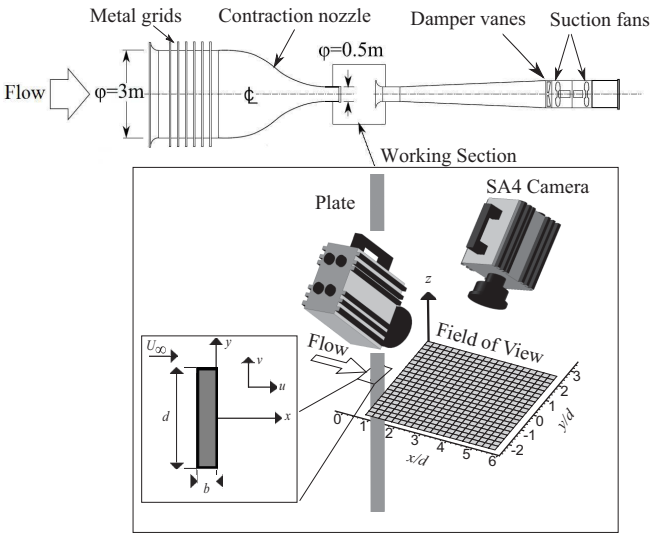

FIG. 1. Schematic of the wind tunnel, stereo-PIV setup, and nomenclature.

The sharp-edged rectangular cylinder models consisted of machine-smoothed aluminium carefully spray-painted matt black to reduce laser light reflections. The models were placed through the center of the working section with one face (of width d) placed normal to the oncoming flow. The models of span $s = 560$ mm extended out of the flow. No end plates were used. The chord d ranged from 12.8 to 13.4 mm, corresponding to Reynolds numbers $6\,500 < Re < 6\,800$ based on d and U_∞. Fifteen rectangular cylinder models of different thickness (b) were used such that $0.05 \leqslant b/d \leqslant 1.92$ as summarized in Table I. The leeward face was at a fixed location 260 mm (approximately $20d$) downstream of the working-section inlet. The thickness was increased upstream of the field of view (FOV), so that the FOV location in the wake was kept fixed relative to the downstream face of the models throughout the measurements.

A tensioning structure ensured the rigidity of the models in the flow. A triple-axis Manfrotto rotary stage enabled accurate adjustment of the plates normal to the oncoming mean flow. The origin of the Cartesian coordinates is the midpoint of the downstream face of the plates at midspan with x in the streamwise direction, y in the cross stream, and z in the spanwise direction as shown in Fig. 1.

Time-resolved stereo-PIV measurements were performed for $0.5 < x/d < 5.5$. The stereo-PIV method is well described [42–45]. The high-frame-rate LaVision system included a Photonics

TABLE I. Overview of rectangular cylinder dimensions. The Reynolds number Re is based on d, $U_\infty = 8.7$ m/s, and ambient conditions of 20 °C, 90 kPa (a).

b/d	d (mm)	b (mm)	Re	b/d	d (mm)	b (mm)	Re
0.05	12.85	0.64	6511	0.44	13.36	5.88	6780
0.07	13.25	0.96	6724	0.53	13.31	7.10	6765
0.11	12.83	1.47	6511	0.59	13.28	7.81	6765
0.20	13.33	2.68	6765	0.78	13.32	10.36	6765
0.25	13.33	3.34	6765	1.00	12.80	12.75	6511
0.30	13.30	3.94	6765	1.53	13.33	20.39	6765
0.34	13.28	4.57	6765	1.92	13.29	25.52	6724
0.38	13.31	5.12	6765				

Industries 20mJ Nd:YLF laser producing a 1.5-mm light sheet to illuminate the seeded flow, and a pair of Photron SA4 Fastcams (1024 × 1024 pixels). Cameras, mounted on a traversing system with equal and opposite angles of 45° relative to the z axis, were focused on the same field as shown in Fig. 1. The Scheimpflug conditions [44] were satisfied through an adapter enabling accurate focus on the skewed planes of view. The flow was seeded with olive oil as tracer particles of roughly 1–2 μm in diameter generated with a Laskin nozzle. Since the reflected laser light from the obstacle surfaces saturates the cameras near the surfaces, it was decided to position the stereo-PIV window downstream of the plate and exclude the plate from the camera view. For each measurement plane, three trials were taken. In each trial, 2 700 snapshots were recorded over 4.5 s in a double-pulse mode. The double-pulse separation was 24 μs and the image-pair acquisition frequency was $f_s = 600$ Hz, which allowed to capture 6 to 10 data points per shedding cycle.

Images were processed using Davis Flow Master 8.2 stereo reconstruction adaptive multi-grid correlation algorithm, which accounted for the distortion and the subpixel window displacement. Calibration followed the empirical three-dimensional (3D) reconstruction of Ref. [46].

Two passes of frame-straddled arrangement-vector processing were performed, in which the interrogation window size was decreased from 64 × 64 at the first pass to 32 × 32 at the second, both with 50% overlap leading to a vector spacing of 14.5 pixels, which represented a spatial grid resolution of 1.1 mm or $0.085d$ in a 78 × 71 mm^2 field of view. Less than 2% (on average) of the vectors were detected as incorrect. The boundaries of postprocessed stereo-PIV images were cropped to exclude the regions of higher uncertainty associated with interpolation at the edges.

In the present arrangement, the particle image was 2.5 × 2.5 pixels on average. According to Ref. [44], the particle images were adequately resolved, and no smoothing or modification of the data was conducted. Subpixel accuracy for the velocity without peak-locking effects was verified through inspection of the bimodal distribution of the particle displacement histograms. Following Ref. [47], the rms PIV velocity error, σ_v, is given by $\sigma_v \approx 0.1(S_{\text{pix}} M_s/\Delta t)$, where S_{pix} is the pixel size, M_s is the scale factor of the image, and Δt is the time step between successive images. In the present experiment, $S_{\text{pix}} = 4$ μm, $M_s = 4.1$, and $\Delta t = 24$ μs. Thus, $\sigma_v = 0.068$ m/s. Based on the procedure detailed by Ref. [48], the estimated overall uncertainty (comprising systematic and random uncertainties) is no greater than 1% and 6% for the normalized mean velocity and Reynolds stresses, respectively, within a confidence interval of 95%. All normalization of the velocity components and Reynolds stresses in this paper is by U_∞ and U_∞^2, respectively.

III. METHODOLOGY

The present flows exhibit low-frequency variations in short-term mean and amplitude of the nearly periodic fluctuations associated with vortex shedding. The generalized phase average (GPA), proposed in Ref. [40], is a refinement of the triple decomposition of Ref. [49]. It draws on concepts of mean-field theory [41] to capture the coherent contribution to cycle-to-cycle variations. The GPA thus allows comparison of the structure of shed vortices for different shedding cycles. In this section, the key concepts and construction of the GPA are briefly summarized.

Starting with the triple decomposition of Ref. [49], the velocity field $\mathbf{u}$ is represented by the summation of a base flow, $\mathbf{u}_B$, a contribution from the large-scale spatially correlated motion, $\mathbf{u}_c$, and uncorrelated residual motion, $\mathbf{u}''$:

$$\mathbf{u}(\mathbf{x},t) = \mathbf{u}_B(\mathbf{x},t) + \mathbf{u}_c(\mathbf{x},t) + \mathbf{u}''(\mathbf{x},t), \tag{1}$$

where bold symbols represent vectorial quantities. In the traditional phase-averaging technique, the base flow is taken to be the mean flow, viz.,

$$\mathbf{u}_B(\mathbf{x},t) = \overline{\mathbf{U}}(\mathbf{x})$$

and $\mathbf{u}_c$ is the conditionally averaged fluctuating component of the flow field according to the shedding phase, ϕ. As shown by Ref. [50] for the analysis of a circular cylinder wake using spatially correlated

PIV measurements, $\mathbf{u}_c$ can be represented by

$$\mathbf{u}_c(\mathbf{x},\phi) = \sum_{i=1}^{2} \tilde{a}_i(\phi)\boldsymbol{\Psi}_i(\mathbf{x}), \tag{2}$$

where $\tilde{a}_i$ are the phase-averaged temporal modal coefficients and $\boldsymbol{\Psi}_i(\mathbf{x})$ are the orthonormal spatial modes. Here, $\boldsymbol{\Psi}_i(\mathbf{x})$ correspond to the spatial functions of the mode pair for the first harmonic of the fluctuating field, associated with the principal (vortex shedding) frequency, as obtained from proper orthogonal decomposition [51]. By construction, the traditional phase average does not account for cycle-to-cycle variations of the fluctuation amplitude since $\tilde{a}_i$ is a function of the shedding phase only, $\phi = \tan^{-1}[a_2(t)/a_1(t)]$, where $a_1(t)$ and $a_2(t)$ are the temporal modal coefficients of the first harmonic pair and the fluctuation amplitude $\sqrt{\tilde{a}_1^2 + \tilde{a}_2^2}$ is constant.

In the GPA, the cycle-to-cycle variations in the shedding process are represented by including a slow-varying contribution to the base flow and envelope of the first harmonic fluctuation amplitude. First, the base flow is defined as the combination of the mean field and a slow-varying mode, denoted by the subscript Δ:

$$\mathbf{u}_B(\mathbf{x},t) = \overline{\mathbf{U}}(\mathbf{x}) + a_\Delta(t)\boldsymbol{\Psi}_\Delta(\mathbf{x}). \tag{3}$$

In this study, $\boldsymbol{\Psi}_\Delta$ corresponds to the most energetic nonperiodic mode for each case considered.

The slow-varying mode is analogous to the slow-drift or shift mode proposed by Ref. [52] to describe the transient growth of instabilities in low-Reynolds-number cylinder wakes. In low-dimensional models, the shift mode is included in the Galerkin projection to describe the energy exchange between the modes for the slowly varying base flow and the first harmonic pair due to the action of the Reynolds stresses [51]. The shift mode is thus related to mean-field theory [41] as it describes the base-flow drift between the unstable steady laminar solutions towards the attractor (dynamically stable oscillatory solution). For low Reynolds numbers, the solution trajectory lies along a (mean-field) paraboloid when plotted in the a_1,a_2 vs a_Δ modal space.

For higher-Reynolds-number turbulent wakes downstream of cantilevered square cylinders [40] and surface-mounted square-based pyramids [53], it has been shown that the solution trajectory in the a_1,a_2 vs a_Δ modal space is scattered about a mean-field paraboloid due to the perturbations caused by the turbulent motion. Thus, in the GPA, the mean-field paraboloid is modeled according to

$$a_\Delta = c_1\left(A_1^{\mathrm{GPA}}\right)^2 + B_{\mathrm{FP}}, \tag{4}$$

where the model coefficients c_1, B_{FP} are found by minimizing the mean square residual between the total flow field and the modeled GPA field. A_1^{GPA} is the modulus of the modeled first harmonic pair such that the GPA coefficients are

$$\langle a_1\rangle = A_1^{\mathrm{GPA}}\cos\phi, \quad \langle a_2\rangle = A_1^{\mathrm{GPA}}\sin\phi, \tag{5}$$

where $\langle\cdot\rangle$ denotes the GPA, ϕ is the shedding phase, and A_1^{GPA} is a function of a_Δ. Hence, in contrast to the traditional phase average of Eq. (2), for the GPA the cycle-to-cycle variation in the amplitude of coherent fluctuations, $\sqrt{\langle a_1\rangle^2 + \langle a_2\rangle^2}$, is represented.

A. GPA construction

The construction of the GPA follows the procedure of Ref. [40] and is briefly summarized for completeness. The inherent symmetry in the fluctuating flow ($\mathbf{u}'$) is exploited in order to accelerate the convergence of modes [51] by splitting them into symmetric and antisymmetric fields across the centerline ($y = 0$) such that

$$\mathbf{u}'(\mathbf{x},t) = \mathbf{u}(\mathbf{x},t) - \overline{\mathbf{U}}(\mathbf{x}) = \mathbf{u}'^s(\mathbf{x},t) + \mathbf{u}'^a(\mathbf{x},t). \tag{6}$$

The components of the symmetric field are defined as

$$u'^{s}(x,y,z,t) = \tfrac{1}{2}[u'(x,y,z,t) + u'(x,-y,z,t)],$$
$$v'^{s}(x,y,z,t) = \tfrac{1}{2}[v'(x,y,z,t) - v'(x,-y,z,t)],$$
$$w'^{s}(x,y,z,t) = \tfrac{1}{2}[w'(x,y,z,t) + w'(x,-y,z,t)],$$

and the components of the antisymmetric field, indicated by the superscript a, are given by modifying the equations above by changing the sign of the second term in the square brackets.

The symmetric and antisymmetric subspaces are orthogonal by construction. In considering the present data set, it is noted that the two most energetic modes in the antisymmetric field represent the first harmonic pair at the principal (vortex shedding) frequency, while the most energetic mode in the symmetric field corresponds to the slow-varying mode.

A Gaussian filter $g(t)$ is applied to the symmetric field to accelerate the convergence of the slow-varying mode. The filtered field is computed as

$$\langle \mathbf{u}'^{s} \rangle_G(t) = \int_{-\infty}^{\infty} (\mathbf{u}')^s(\tau) g(t-\tau) d\tau, \quad \text{where} \quad g(t) = \frac{1}{\sqrt{2\pi}\sigma} \exp\left(-\frac{t^2}{2\sigma^2}\right), \tag{7}$$

and σ is the bandwidth parameter.

Hosseini *et al.* [53] proposed a robust procedure for selecting σ. First, the integral time scale T_Δ of slow-varying motion is estimated as the first zero crossing of the autocorrelation of the temporal coefficients of the slow-varying mode from the unfiltered data. Subject to the Nyquist theorem, the cutoff frequency is then $f_c = 2/T_\Delta$. Letting f_c correspond to the half-power point of the filter, the bandwidth parameter is $\sigma = \sqrt{2\ln 2}/2\pi f_c$. For the cases studied in this work, f_c ranged from $0.12 f_{sh}$ to $0.23 f_{sh}$. A visual inspection was conducted to verify that $\mathbf{\Psi}_\Delta(\mathbf{x})$ for the filtered and unfiltered fields are qualitatively similar. To ensure orthogonality of the modes, the temporal slow-varying coefficient is defined as

$$a_\Delta(t) = (\mathbf{u}'^{s}, \mathbf{\Psi}_\Delta), \tag{8}$$

where $(\mathbf{u}'^{s}, \mathbf{\Psi}_\Delta) = \iint_\Omega \mathbf{u}'^{s} \cdot \mathbf{\Psi}_\Delta \, dxdy$ denotes the inner product in the Hilbert space over the stereo-PIV observation domain Ω [51].

Attention is brought to the sign of $\mathbf{\Psi}_\Delta$. In the general implementation of POD, the sign of the eigenvectors is arbitrary. However, in the context of mean-field theory, the sign of a_Δ (and thus $\mathbf{\Psi}_\Delta$) has a physical interpretation. Briefly, the sign of a_Δ should always point towards the stable oscillatory (average) solution [52,54], such that fluctuation amplitudes for $a_\Delta > 0$ tend to become smaller and for $a_\Delta < 0$ larger. Practically, this condition is satisfied by verifying that the vertex of the paraboloid represents a minimum for a_Δ.

Figure 2 provides illustrative examples of the modal spatial functions in the form of isocontours for each velocity component, their associated sectional streamlines, and spectra of the temporal coefficients for the three most energetic modes for $b/d = 0.05, 1.00$, and 1.92 as obtained from the FOV downstream of the trailing edge. These three modes represent a large contribution to the total fluctuation energy content (57%, 60%, 38% for $b/d = 0.05, 1.00, 1.92$) and thus represent a statistically significant coherent contribution to the flow field fluctuations. The coherent contribution to the spanwise w' fluctuations is very low, indicating that these are poorly correlated with the shedding process. For the square cylinder ($b/d = 1.00$), the power spectral density functions for the harmonic pairs show a narrow distribution about the peak associated with the vortex shedding frequency and a lower contribution of the slow-varying mode to the total fluctuation energy. These observations are interpreted as indicating a lower cycle-to-cycle variation when compared to the other two cases. Conversely, for $b/d = 1.92$ more important cycle-to-cycle variations are expected since the slow-varying mode contribution is relatively large (comparable to the u' contribution), the spectra show a broader energy distribution about the shedding peak and the energy content of the first harmonic pair is significantly lower than for the other cases.

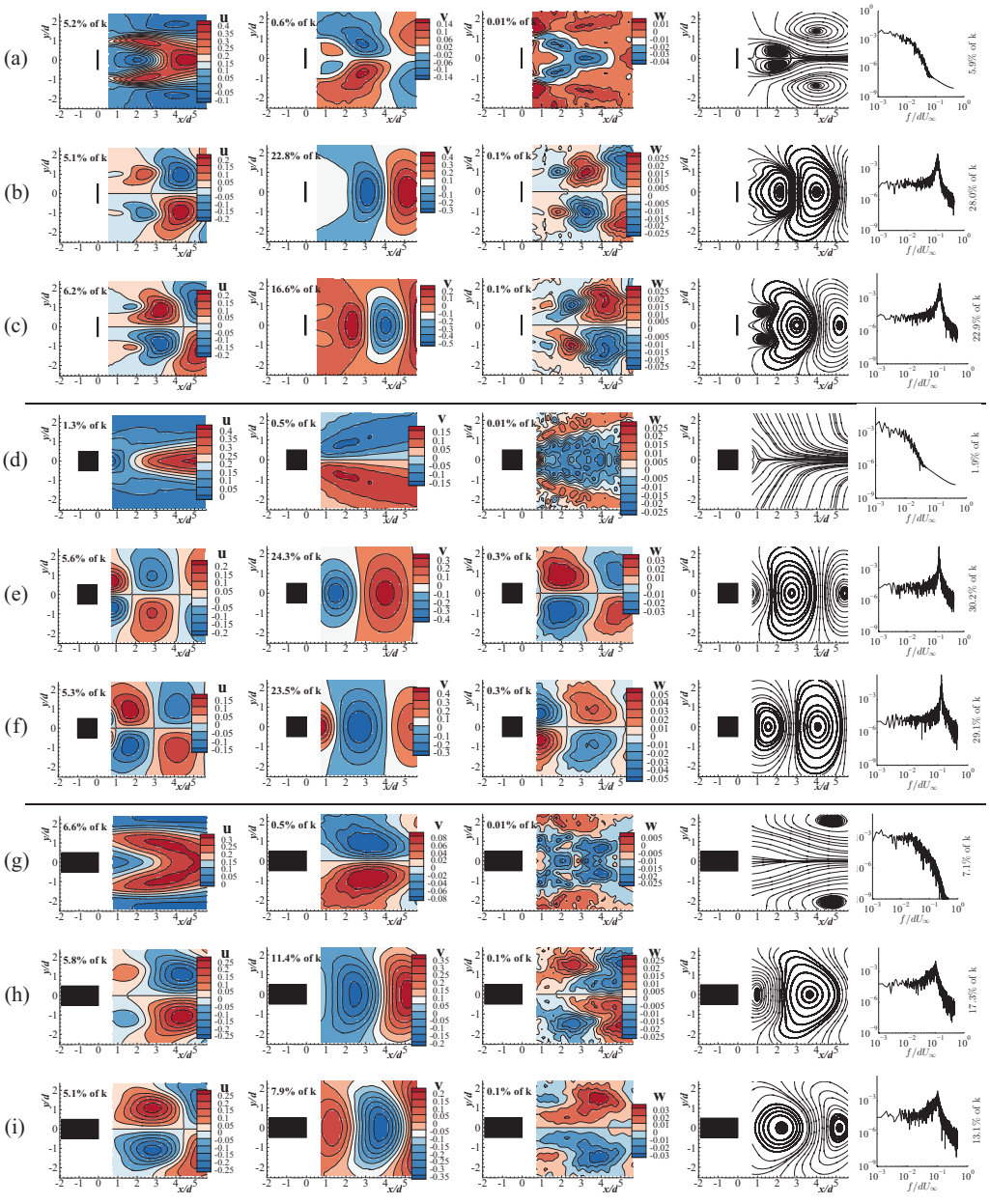

FIG. 2. First three POD coefficients on components of velocity (flow left to right), (u,v) streamlines, and *St* spectrum on their temporal coefficient for $b/d = 0.05$ rows: (a) Ψ_Δ and a_Δ, (b) Ψ_1^a and a_1^a, (c) Ψ_2^a and a_2^a, and in the same order for $b/d = 1.0$ rows (d) to (f) and for $b/d = 1.92$ rows (g) to (i), with percentage of contribution of each to total fluctuation energy $\mathbf{k} = \iint_\Omega k\,dxdy$; Ω denotes the stereo-PIV observation domain. $Re \sim 6\,600$.

The final step is to verify that the behavior of these modes is consistent with the existence of an underlying mean-field paraboloid and then to estimate the parameters c_1 and B_{FP} of Eq. (4). A sample distribution in the modal space confirming a distribution scattered about an underlying paraboloid is shown in Fig. 3 for $b/d = 0.05$.

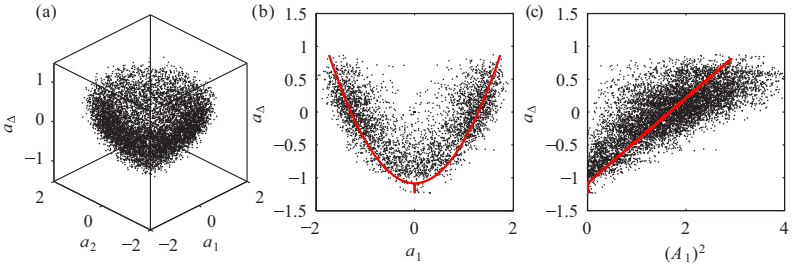

FIG. 3. Example of fluctuations about the mean-field paraboloid in the a_Δ, a_1, a_2 modal space: (a) 3D view of a_Δ vs a_1,a_2; (b) extracted values along $a_2 = 0$ showing fluctuations about the mean-field paraboloid; (c) Distribution of a_Δ vs $A_1^2 = a_1^2 + a_2^2$, A_1 is the amplitude of the first harmonic mode. Red lines indicated the regression as per Eq. (4). Data are shown for $b/d = 0.05$.

In summary, the GPA reconstructs a low-order model of the coherent fluctuating flow field using the shift mode, a_Δ as defined in Eq. (8), and the corresponding phase (ϕ) as inputs to estimate the amplitudes of the first harmonic mode pair, $\langle a_1 \rangle$ and $\langle a_2 \rangle$ modeled on an underlying mean-field paraboloid according to Eq. (5). The GPA model

$$\langle \mathbf{u} \rangle(\mathbf{x},t) = \underbrace{\overline{\mathbf{U}}(\mathbf{x}) + a_\Delta(t)\boldsymbol{\Psi}_\Delta(\mathbf{x})}_{\mathbf{u}_B(\mathbf{x},t)} + \langle a_1 \rangle(t)\boldsymbol{\Psi}_1(\mathbf{x}) + \langle a_2 \rangle(t)\boldsymbol{\Psi}_2(\mathbf{x}) \tag{9}$$

can be reconstructed at any given value of a_Δ to study the vortex structure for different cycle amplitudes. Note that $a_\Delta = 0$ corresponds to the stable oscillatory solution (i.e., the average cycle closely approximating that obtained from a traditional phase average), $a_\Delta > 0$ for cycles for larger and $a_\Delta < 0$ smaller amplitudes compared to the average cycles.

The GPA is a representation of the changes in the shedding cycle due to the slow-varying base flow $\mathbf{u}_B(\mathbf{x},t)$. The base flow variation is expressed through $a_\Delta(t)$, which is considered independent of the shedding phase. Thus, the GPA models the transient response about the stable oscillatory solution. In contrast, the traditional phase average represents only the average amplitude of the periodic fluctuations and thus only the oscillatory motion on the limit cycle.

IV. RESULTS

The turbulent wakes are investigated to document the effect of b/d on the wake structure. For this purpose, the mean wake topology, time-averaged velocities, Reynolds stresses, drag coefficient, and vortex shedding frequency are investigated together with the GPA representation of the shedding process. Global parameters are given for all b/d, but for brevity, detailed presentation of the data is confined to representative cases.

A. The mean field

As a preliminary consideration, the two-dimensionality of the mean flow was verified. Detailed measurements were conducted for the thinnest plate $b/d = 0.05$. In Fig. 4, y profiles of $\overline{U}$, $\overline{V}$, $\overline{u'^2}$, $\overline{v'^2}$, and $\overline{u'v'}$ are shown for several spanwise locations z/d at $x/d = 5.6$. The spanwise velocity, $\overline{W}$, and the Reynolds stresses $\overline{u'w'}$, $\overline{v'w'}$ vanish within the experimental uncertainty and are thus not shown. The distributions at the different z/d are seen to collapse onto single curves within the experimental uncertainty.

Sample results for the spanwise distributions of the maximum values of the Reynolds stresses $\overline{u'^2}$ and $\overline{v'^2}$ at $x/d = 5.6$ downstream of the plate, C_d, St, and mean nondimensional recirculation length x_R, the location x/d along $y = 0$ for which $\overline{U} = 0$, are shown in Fig. 5. The observed variation along

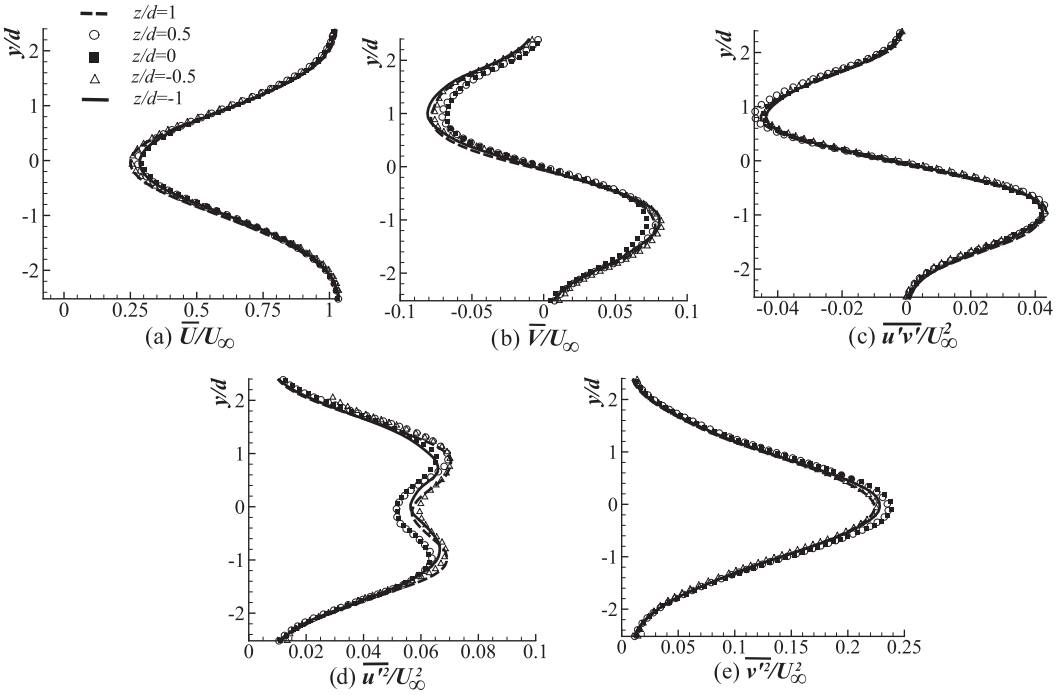

FIG. 4. Mean velocity and Reynolds stress y profiles at $x/d = 5.6$, $Re = 6\,600$ at spanwise locations $z/d = 1, 0.5, 0, -0.5, -1$.

z is within the estimated experimental uncertainty. Less detailed verifications were conducted for several b/d such that the flow may be considered two-dimensional within the allowable experimental variations for the cases considered in this study.

The mean drag was estimated using the slender-wake approximation $[\partial/\partial y(P + \rho\overline{v'^2}) \approx 0]$ according to

$$C_d = \frac{2}{U_\infty^2 d}\left[\int_{-\infty}^{\infty} \overline{U}(U_\infty - \overline{U})dy + \int_{-\infty}^{\infty} (\overline{v'^2} - \overline{u'^2})dy\right] \tag{10}$$

as verified by Ref. [55] for a circular cylinder wake and a thin-airfoil wake by Ref. [56]. In this study, the mean pressure, P, was estimated by solving the Poisson equation over the FOV. Based on P and the measured $\overline{v'^2}$, the accuracy of the slender-wake approximation was found to be good for points

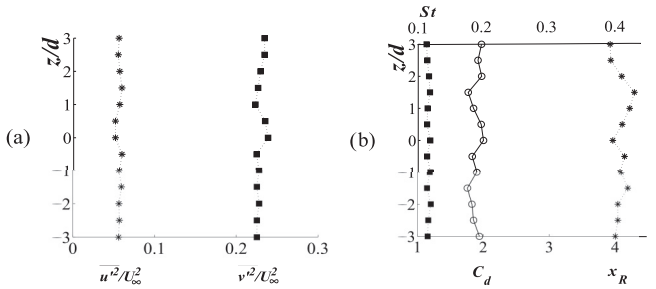

FIG. 5. Spanwise behavior of the mean flow at $Re = 6\,600$. (a) Maximum $\overline{u'^2}/U_\infty^2$ and maximum $\overline{v'^2}/U_\infty^2$ at $x/d = 5.6$, (b) C_d, St, and x_R. C_d estimated using Eq. (10).

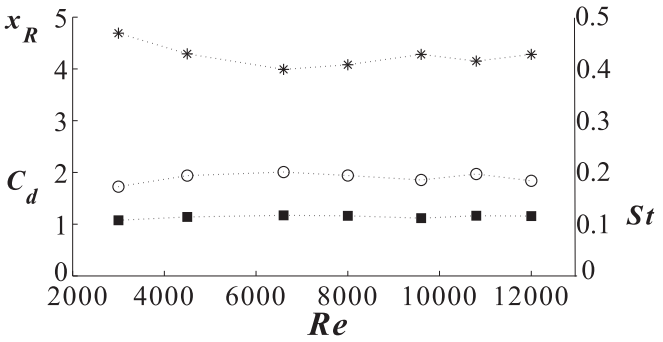

FIG. 6. C_d, St, and x_R as functions of Re for $b/d = 0.05$.

$x/d > x_R + 2$ for all b/d. For $b/d = 0.05$, further experiments in which the FOV was successively moved downstream to $x = 20d$ showed that the approximation continued to be accurate and the calculated C_d changed by less than 2%, which is within the uncertainty of ± 0.04 as estimated from the propagation of the mean field measurement uncertainty.

Additional stereo-PIV experiments at $z = 0$ were conducted for the case $b/d = 0.05$ over the range $3\,000 \leqslant Re \leqslant 12\,000$. These results are summarized in terms of St, C_d, and x_R as functions of Re in Fig. 6. While St is insensitive to Re, an influence of the Reynolds number for $Re < 6\,000$ is observed in C_d and x_R.

The mean near-wake flow is summarized in terms of the velocity vectors and the streamlines in Fig. 7 for all b/d. The coordinate system origin ($x/d = y/d = 0$) is located at the center of the leeward face of the plate. The streamlines were calculated by integrating the 3D velocity data using a modified second-order predictor-corrector integration technique with no smoothing of or modifications to the raw data.

Generally, the mean flow field is symmetric about $y = 0$. Since the mean flow is two dimensional, the recirculation region must be topologically closed. Hence, the separation streamline must terminate at the saddle point **S** marking the maximum downstream extent of the recirculation region ($y = 0, x/d = x_R$). Starting with the thinnest case, $b/d = 0.05$, hereafter called the "thinnest plate", the extent of the recirculation region x_R decreases to a minimum for $0.78 < b/d < 1.0$ (**S** lies slightly upstream of the FOV for $b/d = 0.78$) and increases again. As indicated by Refs. [21] and [39], for $b/d \lesssim 1.7$–2, the mean flow does not reattach on the afterbody. Thus, the recirculation length is better measured from the point of separation (leading edges of the obstacles). The recirculation length $L_R = x_R + b/d$ are compared to x_R in Table II and Fig. 8. L_R initially decreases as b/d increases from 0.05 and reaches a plateau in the range $0.25 < b/d < 0.44$, before decreasing again, reaching a minimum around $b/d = 1$ and increases afterward. This behavior may suggest different regimes or ranges as discussed next in relation to the drag coefficient.

The drag coefficients C_d based on Eq. (10) obtained near the exit of the flow domain at $x/d = 5.6$ are shown in Table II. The results of C_d as a function of the plate thickness are compared with earlier experimental results in Fig. 9(a). The different test parameters for these studies are summarized in Table III. All studies show similar trends. Starting with the thinnest plate, C_d increases with increasing b/d until a critical thickness (at which C_d is maximized) and decreases as b/d further increases.

Quantitatively, the present results agree well with those of Fage and Johansen [2] for the thinnest plate ($C_d = 2.1$ as reported uncorrected for blockage or $C_d = 1.97$ based on the blockage correction reported in Ref. [29]) and lie within the scatter of reported values for $b/d \geqslant 1$. However, significant differences exist in both the critical thickness and the magnitude of C_d for $b/d < 1$. For instance at $b/d = 0.5$, Ref. [26] measured $C_d = 2.2$, Ref. [35] found 2.5, while Ref. [34] reported 1.9 and 2.3 for $Re = 6\,700$ and 67 000, respectively. At $b/d = 0.6$, Ref. [14] reported $C_d = 2.6$, Ref. [16] found 3.0, and Ref. [34] reported 2.2 (at both Re). The reported values of the critical thickness include

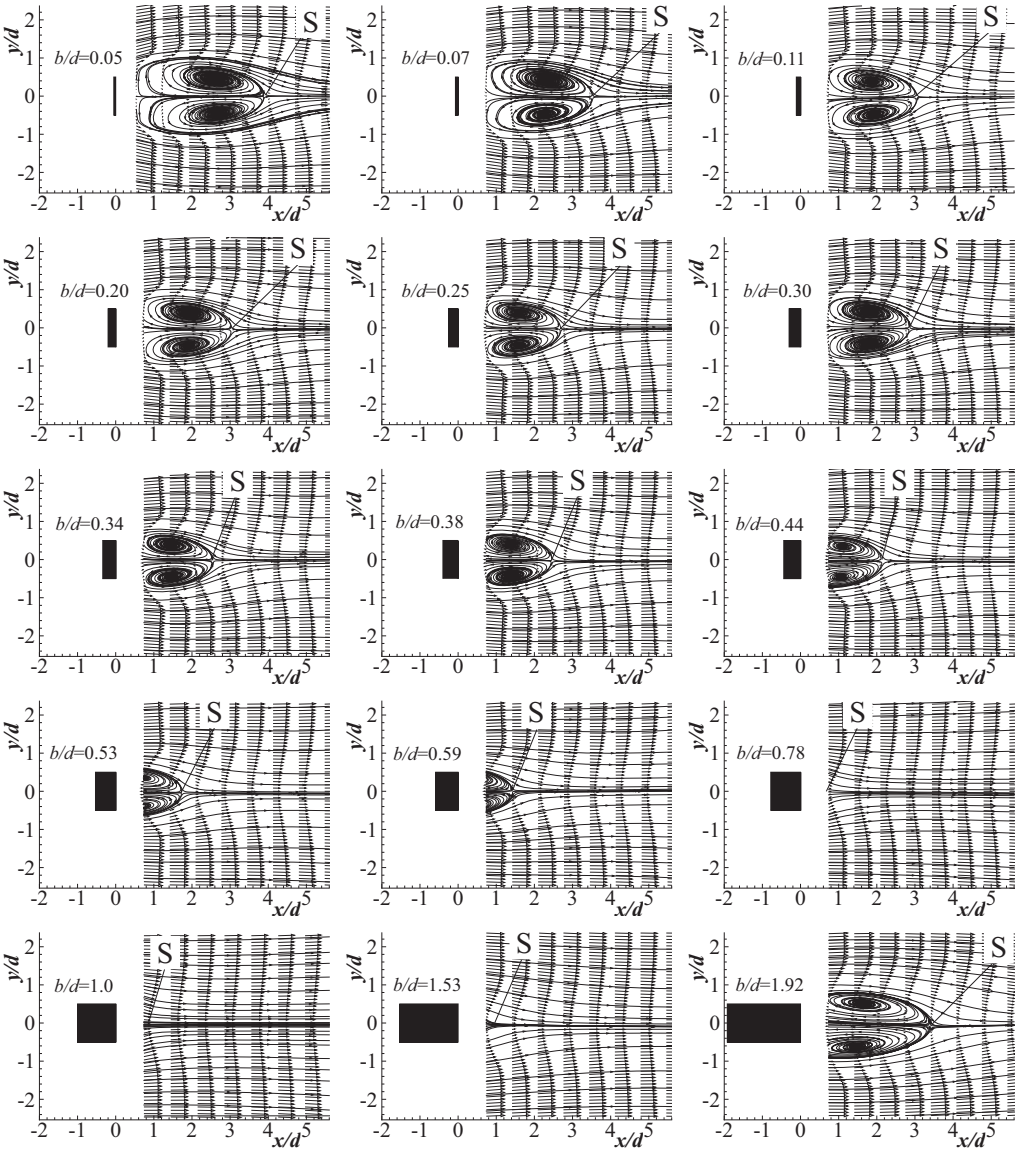

FIG. 7. Mean streamlines and $(\overline{U}/U_\infty, \overline{V}/U_\infty)$ vector field for all b/d measured (flow left to right). $Re \sim 6\,600$.

$b/d = 0.5$ [28,32], $b/d = 0.6$ [21], $b/d = 0.62$ [16], and $b/d = 0.67$ [14,22] while Ref. [34] reports critical values of $b/d < 0.5$ at $Re = 6\,700$ and $b/d \approx 0.7$ for $Re = 67\,000$. In the present work, the critical thickness is found to be approximately $b/d = 0.34$. As is discussed in Sec. V, there is evidence suggesting that the critical thickness is sensitive to the Re and the end conditions.

The mean St in Table II is compared to results from earlier studies in Fig. 9(b). Again, a large scatter is observed between the results of different studies. The present results closely match those of Ref. [20] (at $Re = 6\,700$), Refs. [21] and [23]. Starting from the thinnest plate, St increases monotonically and very slowly as the thickness is increased to $b/d \approx 1.5$. In contrast, Refs. [14] and [22] report a monotonic decrease with increasing b/d, while Refs. [24] and [29] show a decreasing trend for St as b/d is increased to ≈ 0.5 and little change as the thickness is further

TABLE II. Summary of drag coefficient C_d, Strouhal number St, and nondimensional recirculation lengths x_R (measured from back face) and L_R (measured from the front face). $U_\infty = 8.7$ m/s. Estimated uncertainty on C_d is ± 0.04 and on St ± 0.005.

b/d	Re	C_d	St	x_R	L_R $(x_R + b/d)$	x/d for $k_{\max}$	b/d	Re	C_d	St	x_R	L_R $(x_R + b/d)$	x/d for $k_{\max}$
0.05	6511	2.03	0.118	3.82	3.87	4.72	0.44	6780	2.26	0.134	2.12	2.56	2.57
0.07	6724	2.10	0.122	3.51	3.58	4.13	0.53	6765	2.19	0.138	1.73	2.16	1.86
0.11	6511	2.22	0.123	3.02	3.13	3.46	0.59	6765	2.17	0.133	1.41	2.00	1.47
0.20	6765	2.31	0.124	3.02	3.22	3.44	0.78	6765	2.12	0.132	<0.5	<1.5	0.87
0.25	6765	2.42	0.127	2.67	2.92	3.29	1.00	6511	2.00	0.133	0.90	1.90	0.75
0.30	6765	2.41	0.127	2.61	2.91	3.20	1.53	6765	1.78	0.133	0.70	2.23	2.42
0.34	6765	2.42	0.127	2.53	2.87	2.95	1.92	6724	1.71	0.101	3.43	5.35	5.15
0.38	6765	2.34	0.131	2.48	2.86	2.84							

increased. As the thickness approaches $b/d \sim 2$, reported values of St vary widely, possibly due to reattachment of the mean flow on the afterbody as suggested by Ref. [21].

Based on the aforementioned results for the influence of b/d on L_R, C_d, and St, four cases are selected for more detailed analysis: $b/d = 0.05$, representing a thin-plate regime ($b/d < 0.34$); the critical thickness at which C_d is maximized ($b/d = 0.34$); $b/d = 1.00$, representing a cylinder-like (postcritical) regime ($0.34 < b/d \lesssim 1.5$); and $b/d = 1.92$, representing a long-plate regime ($b/d \gtrsim 1.5$). It has been verified that the characteristics of the dynamics and vortex topology for other cases match this classification.

The distribution of the near-wake mean velocities and Reynolds stresses are shown in Fig. 10 as colored isocontours with the streamlines from Fig. 7 for $b/d = 0.05$, 0.34, 1.0, and 1.92. As would be expected for a two-dimensional flow, $\overline{W}$, $\overline{u'w'}$, and $\overline{v'w'}$ are vanishingly small (below the experimental uncertainty) and are thus not shown. Generally, the flow fields are symmetric for $\overline{U}$, $\overline{u'^2}$, $\overline{v'^2}$ and antisymmetric for $\overline{V}$ and $\overline{u'v'}$ about the line $y = 0$.

Qualitatively, the distributions indicated by the isocontours are remarkably similar for $b/d < 1.92$, with regards to the location of the topological critical points (i.e., the recirculation foci and the saddle points). Note that for $b/d = 1.0$, most of the recirculation region lies upstream of the FOV and thus some observations are based on the results of [12]. The $\overline{U}/U_\infty$ contours show the shear layers along

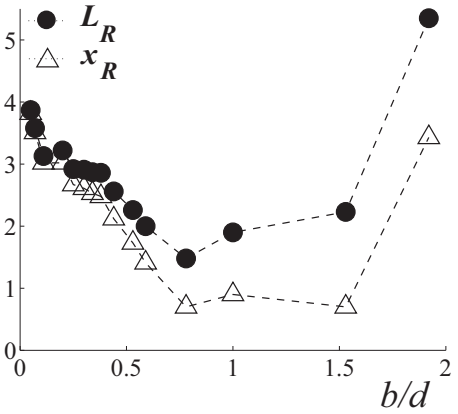

FIG. 8. Mean recirculation length as measured from the obstacle back face x_R and from the front face $L_R = x_R + b/d$ as functions of the obstacle thickness b/d. $Re \sim 6\,600$.

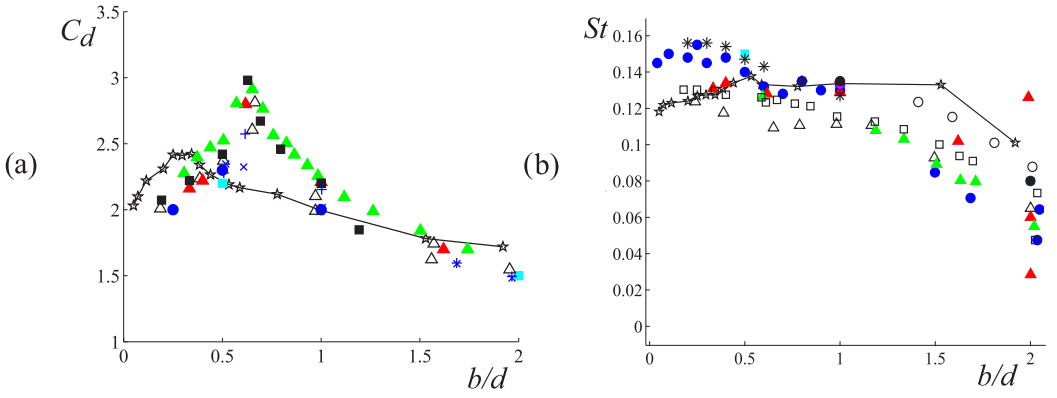

FIG. 9. C_d and St as a function of b/d. Symbols are defined in Table III.

TABLE III. Studies on flow past normal rectangular cylinders. Stereo-PIV; HW, hotwire; SP, surface pressure; FB, force balance.

Reference	Symbol (in Fig. 9)	*Re* (ascending)	Tu (%)	b/d	AR
		(a)			
1, Okajima [21]	●	70–20 000	0.5	1,2,3,4	13.3–100
2, Present study	★	6 600–6 785	0.8	0.05–1.92	38
3, Ohya *et al.* [20]	○	6 700–67 000	0.12	1.5–2.5	7,17
4, Norberg [23]	▲	13 000–30 000	0.06	0.3–5	25
5, Bearman and Trueman [16]	■	20 000–70 000	0.3	0.2–1.2	16
6, Igarashi [22]	□	25 600–57 700	0.5	0.1–4	5, 7.5, 15
7, Nakamura and Hirata [24]	∗	25 000–100 000		0.2–1	4.3
8, Knisely [29]	●	31 000–81 000	0.5	0.04–4	3.2
9, Nakaguchi *et al.* [14]	△	40 000		0.2–4	
10, Courschesne and Laneville [35]	▲	40 000–100 000	0.6	0.3–3	7.2–14.4
11, Vickery [8]	●	40 000–160 000	10	1	14
12, Matsumoto [26]	■	50 000		0.5,2	40
13, Lee [34]	×; AR = 6, +; AR = 20	90 000		0.5,0.6,1.67,2	6–6.7, 20

Ref.	Method	Comment
		(b)
1	HW	No C_d data.
2	Stereo-PIV	
3	HW, SP	No C_d data, blockage uncorrected, low AR.
4	HW, SP	Blockage uncorrected.
5	HW, SP	Blockage corrected.
6	HW, SP, FB	C_d data only for $b/d = 0.5$ and 1, blockage uncorrected, low AR.
7	HW, SP	No C_d data, forced oscillation, blockage uncorrected, low AR.
8	HW, FB	Blockage uncorrected, low ARs, no end plates employed.
9	HW, SP	Blockage uncorrected.
10	FB, SP	Blockage corrected, low AR.
11	FB, SP	No C_d data, high Tu.
12	HW, FB	Blockage uncorrected, forced oscillation.
13	FB	Blockage uncorrected.

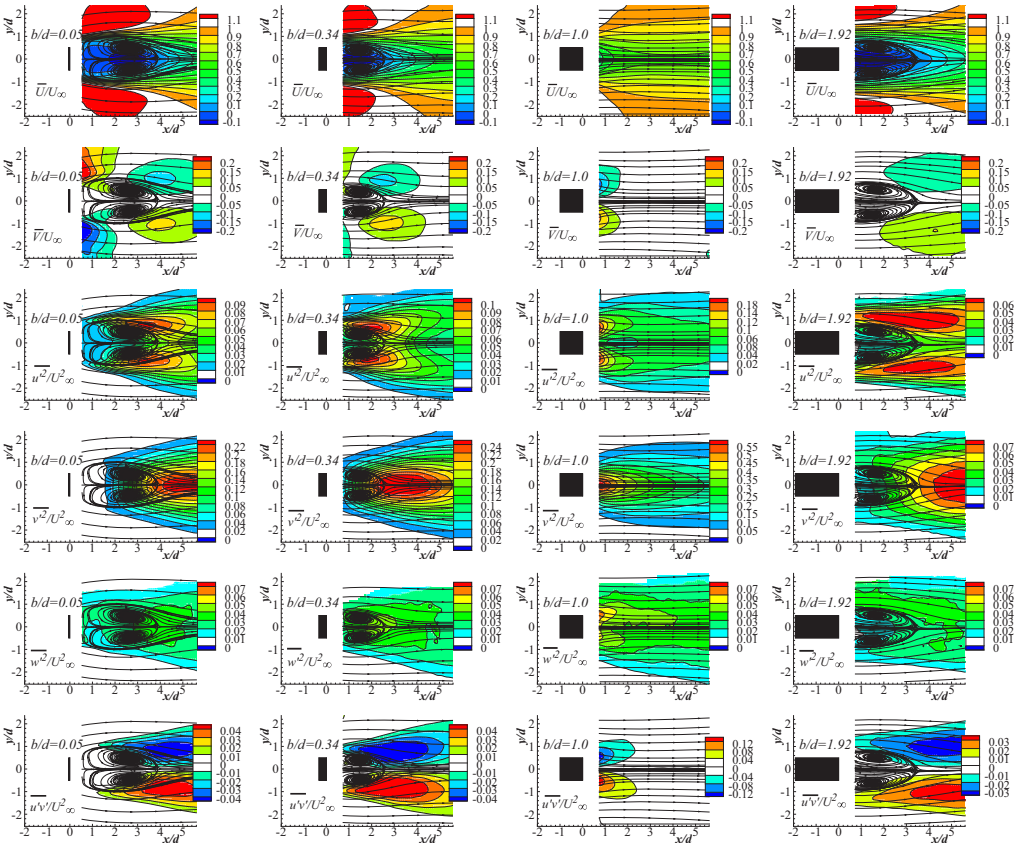

FIG. 10. Contours of mean velocities and Reynolds stresses with mean streamlines for $b/d = 0.05$, 0.34, 1.0, and 1.92. $Re \sim 6\,600$.

the separation streamline and the recirculation zone with negative velocities. Along the symmetry plane $y = 0$, the minimum value for $\overline{U}$ (where $\partial\overline{U}/\partial x = 0$) occurs approximately at the same streamwise location as the center of the recirculation foci. $\overline{V}$ indicates an initial expansion of the recirculation width (the separation streamlines grow further apart in the downstream direction). The distance between the separation streamlines is maximum at approximately the location of the recirculation foci. The maximum gradients $\partial\overline{V}/\partial y$ occur in the vicinity of saddle point (marked **S** in Fig. 7). In contrast, for $b/d = 1.92$, the initial expansion of the wake is not observed and the region of maximum $\partial\overline{V}/\partial y$ occurs significantly downstream of saddle point marked **S** in Fig. 7.

The distribution of the streamwise Reynolds stress ($\overline{u'^2}$) shows a concentration of high levels along the separated shear layer with maxima located slightly downstream of the recirculation foci. Regions of high shear stress $\overline{u'v'}$ roughly coincide with those of high $\overline{u'^2}$ but extend downstream along the edges of the wake. Along the symmetry line, the distribution for $\overline{u'^2}$ shows a maximum close to the location of the saddle point **S** marking the end of the recirculation zone. In this region, the production term for $\overline{u'^2}$ is generally small and negative ($G_{uu} = -\overline{u'^2}\frac{\partial\overline{U}}{\partial x} - \overline{u'v'}\frac{\partial\overline{U}}{\partial y}$; $\frac{\partial\overline{U}}{\partial x} > 0, \overline{u'v'} \to 0, \frac{\partial\overline{U}}{\partial y} \to 0$). Hence, the increase along $y = 0$ is more likely due transport from the separated shear layer as can be surmised from the isocontour pattern.

Concentrations of high levels of the cross-stream normal stress ($\overline{v'^2}$) occur downstream of the recirculation region and the maximum values occur along $y = 0$. In these regions, the magnitude of $\frac{\partial\overline{V}}{\partial y}$ is also very large, giving rise to local maxima in the $\overline{v'^2}$ production rate: $G_{vv} \approx -\overline{v'^2}\frac{\partial\overline{V}}{\partial y}$. The

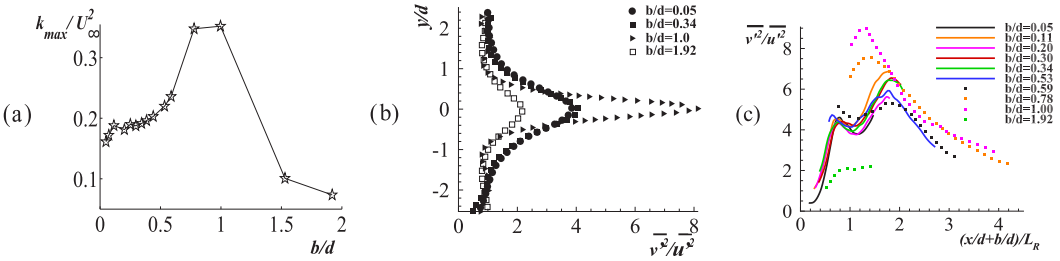

FIG. 11. (a) $k_{\max}$ as function of b/d. The location of $k_{\max}$ along $y = 0$ is given in Table II. (b) y-direction profiles of shape factor, $\overline{v'^2}/\overline{u'^2}$, through $k_{\max}$ points. (c) Shape factor vs $(x/d + b/d)/L_R$ along $y = 0$. $Re \sim 6\,600$.

spanwise normal stress $\overline{w'^2}$ has the smallest magnitude of the three normal stresses. Qualitatively, the distribution of $\overline{w'^2}$ is similar to that of $\overline{v'^2}$, although the maximum occurs between the locations for maximum $\overline{v'^2}$ and $\overline{u'^2}$ along $y = 0$. For a 2D flow, the production term for $\overline{w'^2}$ vanishes identically. Since regions of high levels of $\overline{w'^2}$ coincide those of high $\overline{v'^2}$, the spanwise stresses appear to be generated by an energy exchange from the cross-stream normal stresses through the pressure-strain term.

The magnitude of $\overline{v'^2}$ is significantly larger than that of the other normal stresses. These distribution patterns and differences in magnitude between the Reynolds stresses are similar to those observed for other 2D geometries [12,57] with vortex shedding. For the largest thickness, it is noted that the regions of high level concentrations of the normal stresses are much larger, suggesting a wider wake.

In contrast to the qualitative similarity, the magnitude of the Reynolds stresses differ dramatically as a function of thickness. The changes observed in the magnitude of the fluctuation kinetic energy $k = \frac{1}{2}(\overline{u'^2} + \overline{v'^2} + \overline{w'^2})$ as a function of thickness is representative of the changes seen in the Reynolds stress levels. In regions of large Reynolds stresses, the main contribution to k is $\overline{v'^2}$ such that the maximum value of the kinetic energy, $k_{\max}$, occurs along $y = 0$ close to the location of peak values of $\overline{v'^2}$. From Fig. 11(a), $k_{\max}$ is significantly larger for geometries for which L_R is minimum ($b/d = 0.78, 1.0$) and decreases rapidly for larger obstacles.

The Reynolds stress profiles across the wake at the downstream location for $k_{\max}$ are shown in Fig. 12. Note that for $b/d < 1.92$, these profiles indicate that the width of the wake changes little with thickness, as inferred from the streamline patterns of Fig. 7 and the spatial modes of Fig. 2, whereas for $b/d = 1.92$ the wake is much broader. The magnitude of the Reynolds stresses and the level of anisotropy (the energy distribution amongst the normal stresses) are very similar for $b/d \lesssim 0.6$. For $b/d = 1.0$, there is a significant increase in $\overline{v'^2}$ (comparatively greater than for $\overline{u'^2}$), while levels for $\overline{w'^2}$ change little. Whereas $\overline{v'^2}$ remains the largest contribution to k in the vicinity of $y = 0$, for $b/d = 1.92$ the normal stresses are generally of comparable magnitude. Since $\overline{w'^2}$ levels change little with thickness, the shape factor $\overline{v'^2}/\overline{u'^2}$ provides a fair characterization of the anisotropy levels. Figure 11(b) shows the shape-factor distribution across the wake at the x location for $k_{\max}$ and illustrates the high-anisotropy levels observed for $b/d = 1.0$ and the much lower levels observed for $b/d = 1.92$.

D-shaped, circular, and square cylinder wakes [12,57,58], for which high levels of $\overline{v'^2}$ along $y = 0$ are attributed mainly to the coherent fluctuations due to nearly periodic vortex shedding, are characterized by high levels of anisotropy and large k values immediately downstream of the recirculation region. Hence, considered together, the levels of k, the relatively low levels of $\overline{w'^2}$ and the shape factor provide indicators of the intensity of the fluctuations due to vortex shedding.

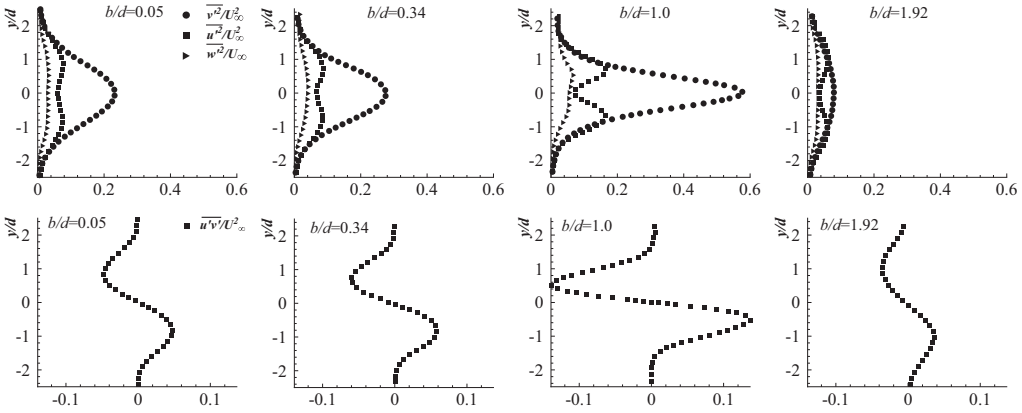

FIG. 12. y-direction profiles through $k_{\max}$ points. Top row: $\overline{v'^2}/U_\infty^2$, $\overline{u'^2}/U_\infty^2$, $\overline{w'^2}/U_\infty^2$. Bottom row: $\overline{u'v'}/U_\infty^2$. $Re \sim 6\,600$.

The shape factor distribution along $y = 0$ is shown in Fig. 11(c) as a function of $(x/d + b/d)/L_R$.[2] Data for some additional b/d are included to clarify trends. It is readily observed that the distribution for $b/d = 1.92$ is very different from that for other obstacles, suggesting different dynamics. For obstacles thinner than the critical thickness $b/d \leqslant 0.34$, it is remarkable that the shape factor distributions nearly collapse on a single double-humped curve. The absolute maximum occurs at approximately $(x/d + b/d)/L_R = 1.8$ and closely matches the location of $k_{\max}$ (or maximum $\overline{v'^2}$). The peak is due to the faster growth of $\overline{v'^2}$ when compared to $\overline{u'^2}$. The local minimum is located close to the end of the recirculation region ($x/d + b/d \sim 1.05L_R$) and arises as $\overline{v'^2}$ decreases while $\overline{u'^2}$ increases as the plate is approached.

The secondary peak (upstream local maximum) occurs in the recirculation zone immediately downstream of the location of the recirculation foci (see Fig. 7). The latter location coincides with that of minimum $\overline{U}$ ($\partial\overline{U}/\partial x = 0$). Between the trough and the secondary peak, $\overline{u'^2}$ decreases faster than $\overline{v'^2}$ when moving towards the plate.

For obstacles of thickness greater than critical ($b/d > 0.34$), the shape factor data no longer collapse on a single curve. For $0.34 < b/d \lesssim 0.78$, the value of the first peak increases while those of the second peak decrease and the trough becomes indistinct. Note that the relative location of the peaks also moves upstream in terms of $(x/d + b/d)/L_R$. For the cases of minimum recirculation ($b/d = 0.78$ and 1.0), the location of maximum $\overline{v'^2}/\overline{u'^2}$ has moved significantly upstream ($x/d + b/d)/L_R \sim 1.3$ and the maximum value is much larger. Reference [12] performed measurements deeper into the recirculation region and found that the shape factor decreases monotonically as the plate is approached. In the latter study, however, it is noted that closest measurement to the cylinder was approximately $d/2$ from the back face.

The disappearance of the upstream (secondary) maximum suggests important dynamic differences. For example, for the thinner obstacles ($b/d < 0.78$), upstream of the minimum $\overline{U}$, $\partial\overline{U}/\partial x < 0$ and $\overline{v'^2}/\overline{u'^2} > 1$, implying a region of negative k production, since along $y = 0$, $\overline{u'v'} = 0$ such that $G_k = (\overline{v'^2} - \overline{u'^2})\frac{\partial\overline{U}}{\partial x}$; noting $\frac{\partial\overline{U}}{\partial x} = -\frac{\partial\overline{V}}{\partial y}$ for a 2D flow. For $b/d = 1.0$, a region of negative production has not been observed in earlier studies and the present distribution for the shape factor is consistent with those studies. In the following sections, the details of the characteristics and process of vortex shedding in the wake are investigated in light of these observations.

[2]When nondimensioned by x_R, the scatter of the peak locations increases.

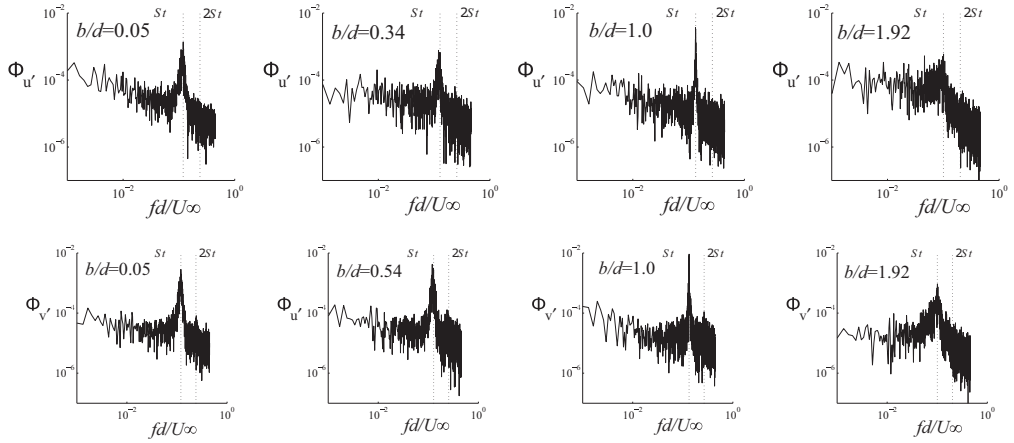

FIG. 13. Power spectral density functions, Φ, for total fluctuations (u',v') at point $(x/d,y/d)=(5,1)$ in the wake of $b/d=0.05$, 0.34, 1.0, and 1.92. Abscissa is the nondimensional frequency fd/U_∞, $Re\sim 6\,600$.

B. Shedding process and coherent cycle-to-cycle variations

In this section, the characteristics of the nearly periodic wake velocity fluctuations are described in terms of the power spectra and envelope of the amplitude modulation of the velocity fluctuations. The GPA is then used to investigate the wake structure for different amplitude shedding cycles.

Figure 13 shows the power spectral density functions (psdf) $\Phi_{u'}$ and $\Phi_{v'}$ for the u' and v' fluctuating velocity components, respectively. The abscissa represents the nondimensional frequency fd/U_∞. The psdf are not normalized; thus, $\overline{u'^2}=2\pi\int_0^\infty \Phi_{u'}(f)\,df$, $\overline{v'^2}=2\pi\int_0^\infty \Phi_{v'}(f)\,df$ as per Parceval's identity. The spectra are shown for $(x/d,y/d)=(5,1)$ for $b/d=0.05$, 0.34, 1.0, and 1.92. The Strouhal frequency is assumed to be that of the maximum Φ giving the values tabulated in Table II for all b/d. As expected for a 2D mean flow, the spanwise fluctuations are poorly correlated with the shedding process and their spectra do not show peaks as those observed in Fig. 13. Hence, these spectra are not shown for brevity.

For $b/d<1.92$, $\Phi_{u'}$ and $\Phi_{v'}$ show well-defined peaks centered about the mean shedding frequency St (the principal harmonic). A weak second harmonic ($2St$) can be observed, which is expected since the measurement points are deep within the wake and thus ostensibly between the counter-rotating vortex streets; see, for example, Refs. [52] or [40]. For $b/d=1.0$ (and 0.78), the spectral peaks are very sharp, suggesting that the fluctuation amplitudes have low modulation and the shedding frequency changes little between cycles. As the thickness is decreased, the fluctuating energy distribution becomes broader about St, suggesting more cycle-to-cycle variation.

In contrast, the broadest spectral distribution occurs for $b/d=1.92$, where the peak levels are much lower than observed for smaller b/d. Moreover, there appears to be a very weak concentration around approximately $\frac{1}{2}St$. Similar spectral distributions were observed by Refs. [21] and [29] for $b/d=2.0$, Ref. [22] in the range of $2.3<b/d<2.8$, and Ref. [38] between $2.0<b/d<2.8$. Reference [38] observed that as Re was decreased to 1000, two peaks first appear in the spectra for $b/d\sim 2.8$–3. These observations have been related to the intermittent reattachment of the shear layer on the afterbody and the Reynolds number dependence is attributed to the state of the redeveloping boundary layer.

Further insight can be gained in interpreting the spectral broadening in relation to some aspects of the wake dynamics by considering the characteristics of the fluctuating velocity signals as illustrated in Fig. 14. In this figure, arbitrarily chosen time sequences of the fluctuating cross-flow component velocity $v'(t)$ taken at the location of $k_{\max}$ are analyzed and compared for $b/d=0.05$, 0.34, 1.0, and 1.92. For each case, the subplots show (a) the time sequence for the slow-varying POD modal

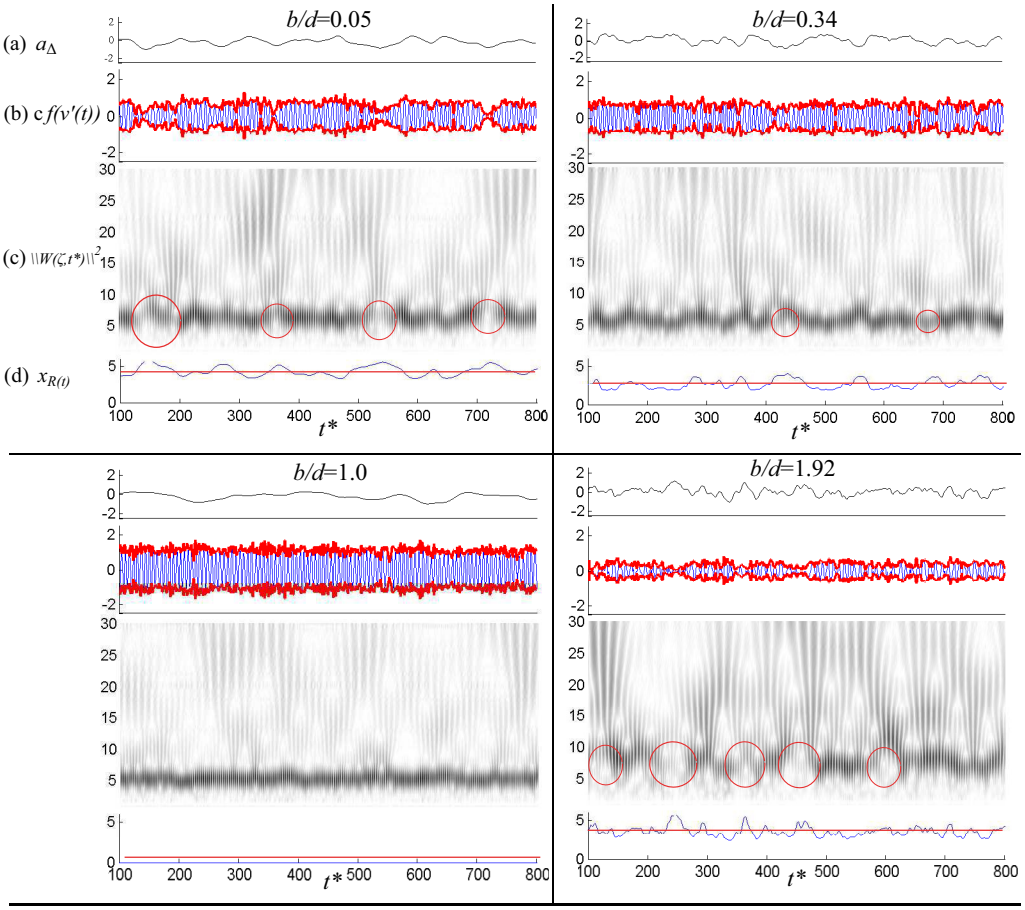

FIG. 14. For each b/d, the plots from top to bottom are (a) a_Δ; (b) Hilbert envelope function [59] $cf[v'(t)]$ (red) of $v'(t)$ (blue) at $k_{\max}$; (c) Morlet wavelet coefficients ($\|\mathcal{W}(\zeta,t^*)\|^2$) of $v'(t)$ with the red circles marking examples of a decrease in vortex shedding amplitude; and (d) instantaneous $x_R(t)$ with red straight line marking the mean x_R value, versus the nondimensional time (t^*). $Re \sim 6\,600$.

coefficient $a_\Delta = (\mathbf{u}', \Psi_\Delta)$ as defined in Sec. III A; (b) $v'(t)$ in blue and envelope of the fluctuation amplitude as estimated from a Hilbert Transform, cf. Ref. [59]; (c) the correlation map obtained from a Morley wavelet (Morlet) transform of $v'(t)$; and (d) the instantaneous recirculation length $x_R(t)$ along $y = 0$, where the red line marks the average recirculation length, i.e., $x_R = \overline{x_R(t)}$. The common abscissa is the time t^* nondimensioned by the sampling rate f_s. The red circles in the figure indicate intervals of very low amplitude fluctuations.

The Morlet used is

$$\psi(t^*) = e^{-t'^2/2}\cos(5t'),$$

where $t' = t^*/f_s(1/T_w)$ and T_w is the measurement window. The wavelet transform is then defined as

$$\mathcal{W}(\zeta,t^*) = \frac{1}{|\zeta|^{1/2}}\int_{-\infty}^{\infty} v'(\tau)\psi\left(\frac{\tau - t^*/f_s}{\zeta}\right)d\tau,$$

where ζ is the scaling factor (inversely proportional to the frequency). Analogously to the Fourier transform, $\|\mathcal{W}\|^2$ is interpreted as the power density at a given scale ζ (the vertical axis of the wavelet correlation maps) at a given time t^*.

Consider the cases $b/d = 0.05$ and 0.34. As b/d is reduced below 1.0, the modulation of the fluctuation amplitude increases. Correspondingly, the fluctuation levels in a_Δ also increase, which is consistent with the increase in the spectral content of this mode, relative to $b/d = 1.0$. Compare, for example, the specta of a_Δ for $b/d = 0.05$ in Fig. 2(a) and for $b/d = 1.0$ in Fig. 2(d). For $b/d = 0.05$, the fluctuation energy contained in the slow-varying mode accounts for approximately 6% of the total fluctuation energy (i.e., $\mathbf{k} = \int\int_\Omega k\, dxdy$; Ω denotes the stereo-PIV observation domain), whereas for $b/d = 1.0$, the fluctuation content for a_Δ accounts for only about 2% of $\mathbf{k}$. There is also a direct correspondence between a_Δ and the instantaneous recirculation length $x_R(t)$ and thus it follows that the slow-varying mode corresponds to the base-flow fluctuation. For large amplitude cycles ($a_\Delta > 0$), $x_R(t)$ is less than the average x_R and when $a_\Delta < 0$, it is longer. In particular, when a_Δ approaches a minimum ($a_\Delta^{\min}$), $x_R(t)$ approaches a maximum. These very low amplitude cycles are circled red in the figure for identification and it is observed that these events occur more frequently as b/d is reduced from 1.0.

The occurrence and duration of these $a_\Delta^{\min}$ events are irregular. In considering the correlation maps of the wavelet transforms, as a_Δ changes, the concentration of high $\|\mathcal{W}\|^2$ changes. During high-amplitude cycles, the length scale decreases (shedding frequency increases) and during low-amplitude cycle the shedding frequency decreases. Thus, the modulation of the shedding frequency increases as the b/d is reduced. This observation is consistent with the increased spectral broadening observed in Fig. 13 [and for the first harmonic in Figs. 2(b) and 2(c) compared to Figs. 2(e) and 2(f)] as the thickness is reduced from $b/d = 1.0$. In particular, as the slow-varying mode approaches $a_\Delta^{\min}$, the energy density distribution changes significantly and $\|\mathcal{W}\|^2$, at the scale corresponding to the shedding frequency, decreases significantly indicating a loss of the periodic nature of the signal. This behavior is interpreted as a disruption of the vortex shedding process. During these instances, the recirculation region is significantly longer than average.

Considering the case $b/d = 1.0$, the fluctuation amplitude is mildly modulated and periods of low-amplitude fluctuations are not observed. They do occur in much larger records, but randomly and very infrequently and it would distort the significance of the record that is shown to display an example. The wavelet map shows a concentration of high correlation values of $\|\mathcal{W}\|^2$ at the scale corresponding to the shedding frequency. The magnitude of $\|\mathcal{W}\|^2$ at this scale varies little in time, indicating that the shedding frequency is very weakly modulated, which is consistent with the very sharp peak observed for the square cylinder in the spectra of Fig. 13 and of the first harmonic POD modes in Fig. 2. Recalling that $a_\Delta = 0$ corresponds to the attractor (i.e., the stable oscillatory solution and thus approximately the average shedding cycle), the coefficient fluctuations about zero are much smaller than observed for smaller b/d. Note that for $a_\Delta > 0$, the fluctuation amplitude is slightly larger and, conversely for $a_\Delta < 0$ slightly smaller, than the average amplitude and thus the cycle-to-cycle variations are not negligible.

The flow at $b/d = 1.92$ exhibits different characteristics showing significantly smaller magnitude $v'(t)$ (and other fluctuating velocity components, not shown). The amplitude of the fluctuations is much more modulated when compared to other cases. Most striking is the significant number of very low amplitude cycles (indicated by red circles) and the higher fractional time spent in those (see Morlet correlation maps). For this thickness, the variations of a_Δ and $x_R(t)$ also increase substantially when compared to smaller b/d. The wavelet correlation maps also show an increase in the cycle-to-cycle variation of the shedding frequency consistent with the spectra of Fig. 13. The low-frequency energy content in the a_Δ spectra of Fig. 2(g) is also increased over a larger frequency band. There appears to be an increase in the energy concentration (magnitude of $\|\mathcal{W}\|^2$) for scales about half the shedding frequency, which is perhaps related to a weak fluctuation energy concentration in the spectral distribution observed around $f_{sh}/2$ in the first harmonic spectra of Figs. 2(h) and 2(i). These observations suggest that the shedding process is less organized.

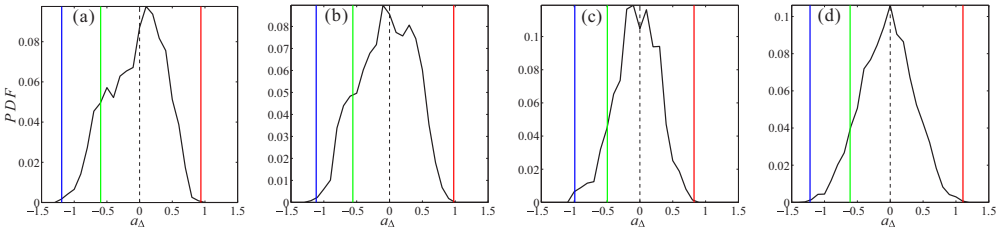

FIG. 15. Probability density function (PDF) for the slow-varying modal coefficient a_Δ for four different b/d. For each thickness, $a_\Delta = B_{FP}$ indicates the location of the paraboloid vertex: (a) $b/d = 0.05, B_{FP} = -1.1$; (b) $b/d = 0.34, B_{FP} = -1.5$; (c) $b/d = 1.0, B_{FP} = -1.6$; (d) $b/d = 1.92, B_{FP} = -0.86$. Broken line indicates $a_\Delta = a_\Delta^0 = 0$; blue line 5% probability a_Δ^{min}; red line a_Δ^{max}; and green line $a_\Delta^{low} = \frac{1}{2}(a_\Delta^{min} + a_\Delta^0)$.

The probability density function (PDF) for the slow-varying mode a_Δ is shown for the cases $b/d = 0.05, 0.34, 1.0$, and 1.92 in Fig. 15. Recall that the amplitude of the first harmonic (the cycle amplitude) is directly related to a_Δ. In this figure, the typical or average amplitude cycle corresponds to $a_\Delta = a_\Delta^0 = 0$ (broken line). Cycles with amplitude larger than average occur for $a_\Delta > 0$ and those with smaller amplitudes occur for $a_\Delta < 0$. Values of a_Δ corresponding to the maximum amplitude cycles (a_Δ^{max}) are indicated by a red line. Approximately 5% of PIV realizations (snapshots) have values $a_\Delta < a_\Delta^{min}$ (indicated by a blue line). The green line corresponds to $a_\Delta^{low} = \frac{1}{2}(a_\Delta^{min} + a_\Delta^0)$ and will be used to represent a typical low-amplitude cycle in the following discussion.

From the PDF distributions for a_Δ, it is observed that the low-amplitude cycles occur with increasing probability as b/d is decreased from 1.0. This observation agrees with those made from the Hilbert and Wavelet transform analyses of Fig. 14. For $b/d = 0.05$ in Fig. 15(a), approximately 5% of events occur for $a_\Delta < a_\Delta^{min} \approx B_{FP} = -1.1$ and thus lie below the paraboloid vertex. During these events, the energetic contribution of the first harmonic is negligible and thus these events are interpreted to imply an interruption of vortex shedding activity. For $b/d = 0.34$ [the critical thickness, Fig. 15(b)] very low amplitude cycles (a_Δ approaches $B_{FP} = -1.5$) are observed for which the vortex shedding activity is very weak. For $b/d = 1.0$ [Fig. 15(c)], the PDF is symmetric about a_Δ^0 and a_Δ^{min} is significantly larger than $B_{FP} = -1.6$, indicating continuous and sustained shedding activity. For $b/d = 1.92$ in Fig. 15(d), a very large number of interruptions in shedding cycle ($a_\Delta^{min} < B_{FP} = -0.86$) are observed. As is shown below, the shedding dynamics for $b/d = 1.92$ differ from those for the thinner plates in several respects.

The wake structure is investigated next using the GPA at four representative fluctuation amplitudes. The high-amplitude cycles are represented by the largest positive value of the slow-varying coefficient, denoted a_Δ^{max}, and the typical or average amplitude cycle by events with $a_\Delta = 0$, denoted by a_Δ^0. Very low amplitude cycles, or intervals when shedding activity is interrupted, are represented by $a_\Delta = a_\Delta^{min}$ and a typical low-amplitude cycle is represented by $a_\Delta = a_\Delta^{low}$, noting that in both latter cases $a_\Delta < 0$.

Figure 16 shows the wake for approximately the same shedding phase ϕ (approximately when the top vortex is shed) corresponding to a_Δ^{max}, a_Δ^0, a_Δ^{low}, and a_Δ^{min} for $b/d = 0.05$, 0.34, 1.0, and 1.92.[3] The raw stereo-PIV field at this instant is shown together with the GPA representation. The in-plane vector components correspond to $\langle u \rangle$ and $\langle v \rangle$ following Eq. (9). The flooded isocontours represent the vorticity ($\omega_z = \partial v/\partial x - \partial u/\partial y$ for the normalized raw field and $\langle \omega_z \rangle = \partial \langle v \rangle / \partial x - \partial \langle u \rangle / \partial y$ for the GPA field). The solid lines enclose the vortex cores as identified using the second-invariant or Q criterion ($Q = 0.01$).

[3]For the cases $b/d = 0.05$ and 1.92, time intervals around $a_\Delta^{min} < B_{FP}$, the phase ϕ has no physical meaning, since the shedding cycle is interrupted.

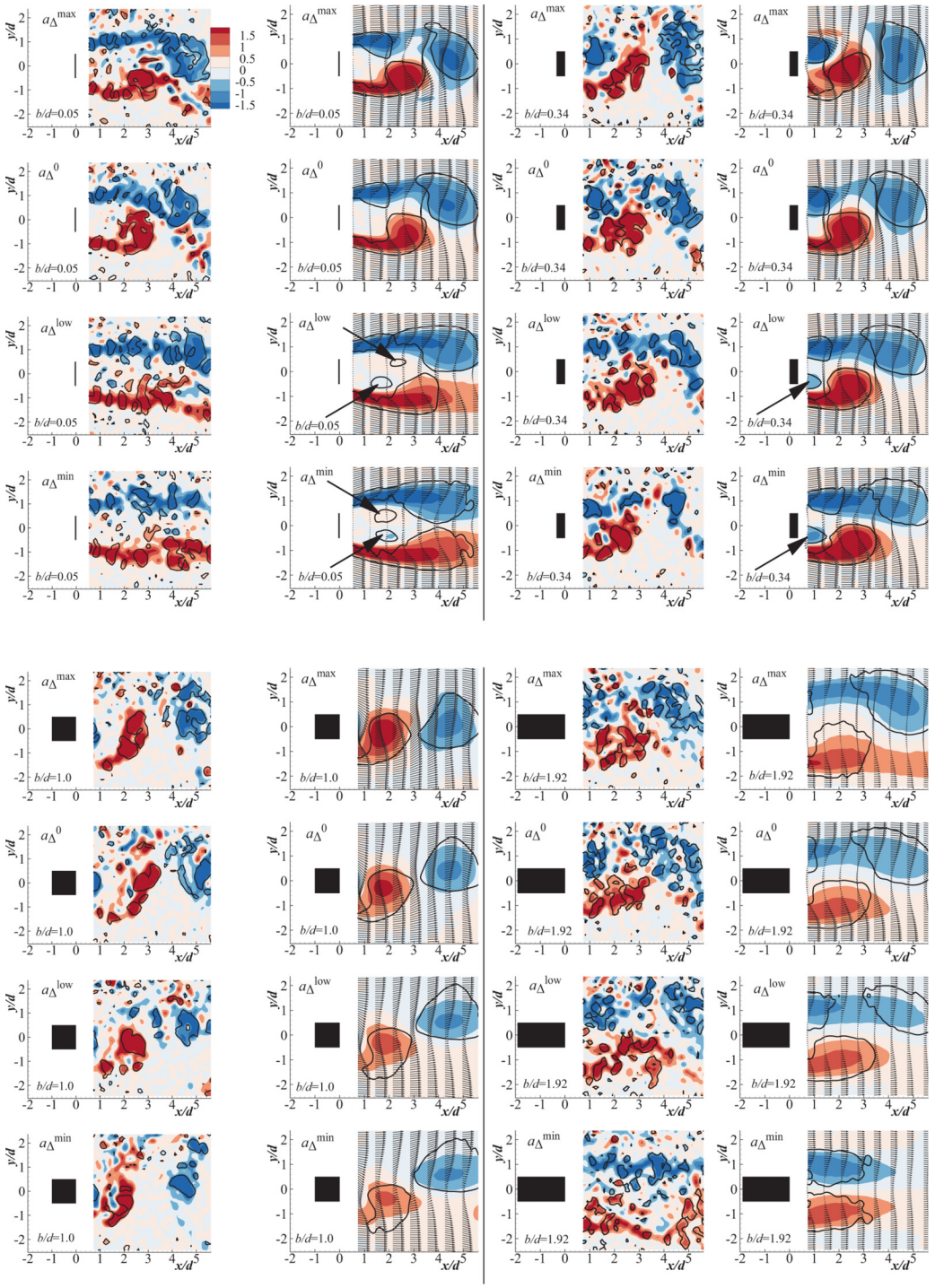

FIG. 16. Vortex shedding at a_Δ^{max}, a_Δ^{0}, a_Δ^{low}, and a_Δ^{min} for $b/d = 0.05, 0.34, 1.0$, and 1.92 ($Re \sim 6\,600$): First and third columns show the instantaneous flow field with contours of ω_z and lines of $Q = 0.01$; second and fourth columns show GPA model with contours of $\langle\omega_z\rangle$, lines of $Q = 0.01$ and vector field $(\langle U\rangle/U_\infty, \langle V\rangle/U_\infty)$. The contour levels are the same in each frame. The arrows are explained in the text.

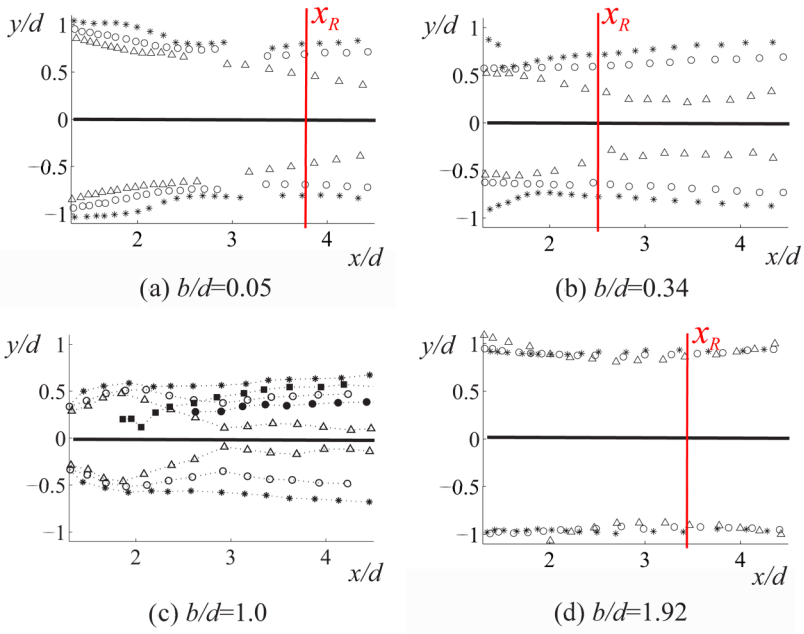

FIG. 17. Vortex core locations in phase sequence at $a_\Delta^{\max}$, △; a_Δ^0, ○; and a_Δ^{low}, ∗. $Re \sim 6\,600$. Data for $b/d = 1.0$ is compared with Ref. [12], ■; and Ref. [57], ●. The vertical red lines show the end of the recirculation zone.

The case $b/d = 1.0$ shows the least modulation of the fluctuation amplitude or variation in a_Δ and is thus discussed first to provide a comparison for other cases. In Fig. 16, the coherent contribution to the vorticity field rendered by the GPA represents fairly well the instantaneous raw data field. As expected, the vortex cores shown in the GPA contain high concentrations of the coherent vorticity. As a_Δ decreases, it is noted that these high-vorticity regions are increasingly deformed (stretched streamwise) and the downstream (cross-flow) separation of the centroids appears to increase.

The trajectories of the centroids of the shed vortices from the GPA are compared for the different amplitude cycles in Fig. 17. The centroids correspond to the location of the peak vorticity; cf. Ref. [12]. The trajectory for $a_\Delta = 0$ corresponds well to those reported for the average (i.e., that obtained from a traditional phase average) as reported for a square cylinder [12] and circular cylinder [57] wakes. For low-amplitude cycles, the centroid trajectory leads away from the symmetry line $y = 0$, whereas high-amplitude cycles leads towards it. Note that the trajectory for the different cycles start diverging roughly d downstream of the formation region.

The circulation contained in the shed vortices is shown in Fig. 18. The circulation is estimated from $\Gamma_c = \int\int \langle \omega \rangle \, d\mathbf{A} = \int\int \langle \omega_z \rangle \, dxdy$. The integration is carried out over a contiguous vorticity domain for $Q > 0.002$.[4] For $b/d = 1.0$, the initial circulation is larger (stronger vortices) for high-amplitude cycles than for lower amplitude cycles, but these differences vanish rapidly downstream. The present results agree well with those reported for the phase-averaged cycles [12]. Hence, it appears that the high fluctuation levels [$k_{\max}$ in Fig. 11(a)] observed for $b/d = 1.0$ are a result of induction by the vortices and are more related to the trajectory of these vortices than their strength.

As the thickness is reduced, the wake structure between cycles differs increasingly (Fig. 16). Considering the high-amplitude $a_\Delta^{\max}$ cycles for $b/d = 0.05$ and 0.34, the selected phase is seen

[4]In the calculation for Γ_c, the lower limit of Q was progressively reduced until an asymptotic behavior was observed.

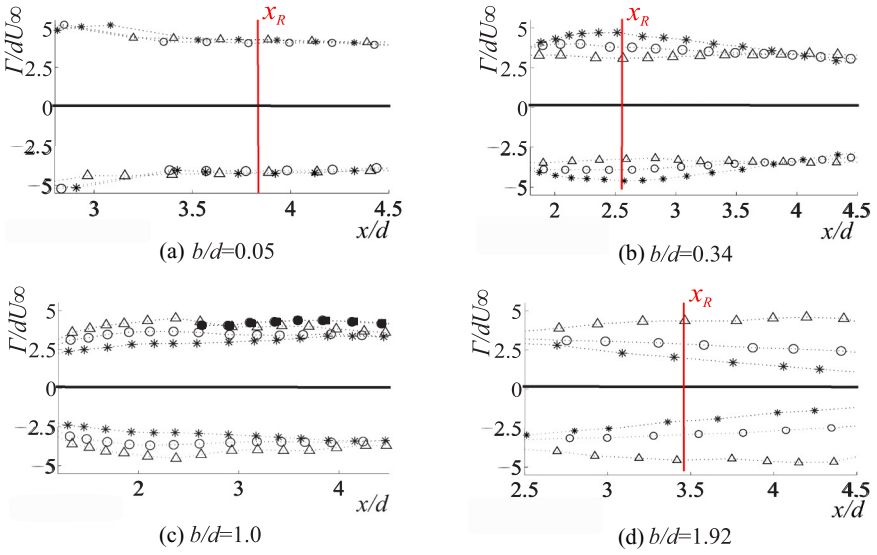

FIG. 18. Circulation (Γ_c/dU_∞) of vortices in phase sequence, vs streamwise core locations (x/d) at $a_\Delta^{\max}$, $\triangle$; a_Δ^0, $\circ$; and a_Δ^{low}, $*$. $Re \sim 6\,600$. Data for $b/d = 1.0$ is compared with Ref. [12], ■. The vertical red lines show the end of the recirculation zone.

to correspond approximately to the instant when the top vortex is shed, when the vortex detaches from the feeding shear layer. Again, the coherent field represented by the GPA appears to capture well the dominant features observed in the raw field for the four cycles shown. In general, the recirculation and formation regions increase as a_Δ and, thus, the fluctuation amplitude decrease, which is consistent with earlier observations for thin plates [36,37].

Attention is focused next on the cycles $a_\Delta^{\max}$,a_Δ^0, and a_Δ^{low}. For $b/d = 0.34$, during high-amplitude cycles, $a_\Delta^{\max}$, the vortex—forming as the bottom (red) shear layer rolls up—penetrates deeply into the wake and interrupts the flux of vorticity along the upper shear layer (blue) as described in the classical vortex shedding model [60].

In contrast, as a_Δ decreases, the separated shear layer remains attached to the shedding vortex even though these constructions are shown at similar shedding phases ϕ. This vorticity distribution is also noted in the raw field. The bottom shear layer does not roll up as deeply into the wake and interferes less with the upper shear layer, allowing strands of vorticity connecting the forming and shed vortices to appear. The vorticity concentration along the strands increases as a_Δ decreases. Similar observations are made for $b/d = 0.05$, albeit the vorticity flux along the strands is generally greater and the low-amplitude cycles occur more frequently than for $b/d = 0.34$.

From the wavelet correlation maps of Fig. 14, the shedding frequency is lower (larger scale) during low-amplitude cycles when compared to high-amplitude cases, which suggests that in the presence of the strands the shedding of vortices is delayed. Moreover, an increase of energy content at the largest scales is also observed. As described by Ref. [61], the roll-up of the opposing shear layer interrupting the vorticity flux to the forming vortex is important to maintaining the regularity of the vortex shedding clockwork. The presence of the strands and increased energy content at larger scales (low-frequency range) implies a disturbance to this clockwork and thus would be consistent with earlier observations [36,37] for thin plates: The structure of the shed vortices appears less regular during low-amplitude cycles and these low-amplitude events can be associated with a low-frequency spectral signature.

The trajectory of the centroids are remarkably similar to those observed for $b/d = 1.0$, see Fig. 17, even though the trajectories for different amplitude cycles deviate earlier, with respect to x_R, as the thickness is reduced. The circulation of the shed vortices (for $x/d > x_R$ in Fig. 18) is very similar

for all cycles. Perhaps surprisingly, Γ_c changes little with the thickness as long as the separating shear layer does not reattach on the afterbody (as occurs for $b/d = 1.92$).

Consider next the lowest amplitude cycles, denoted by $a_\Delta^{\min}$. For $b/d = 0.34$, $a_\Delta^{\min}$ in Fig. 15(b) lies very close to the vertex of the estimated mean-field paraboloid. Vortices are still shed but the frequency is irregular; the wavelet correlation coefficients in Fig. 14 indicate that the energy at the nominal shedding frequency is very low. For $b/d = 0.05$ [Fig. 15(a)], $a_\Delta^{\min}$ lies below the paraboloid vertex; thus the GPA represents these events as interruptions in the vortex shedding cycle and the fluctuations are those of the base flow. The raw field is consistent with this observation; the separated shear layer extends far downstream and does not show evidence of the typical roll-up associated with the vortex formation and shedding process. These events of disrupted shedding occur more frequently as the thickness is reduced and appear to correspond well to the disorganized wake regimes described in the earlier literature.

A peculiar secondary feature is observed for the low-amplitude shedding cycles for $b/d = 0.05$ and 0.34. A region of counter-rotating vorticity (blue, indicated by an arrow in Fig. 16) occurs near the lower shear layer vorticity (red). Since the GPA represents the coherent contribution to the fluctuating field, it is not surprising that this feature is observed in the raw field as well. Moreover, it has been verified that a similar feature is observed at the root of the upper shear layer in the second half of the shedding cycle, i.e., 180° later than the shedding phase shown in the figure. The vorticity concentration associated with this secondary feature increases as a_Δ decreases. Its circulation would induce a motion opposing that of the roll-up of the shear layer. It may thus represent, at least in part, the mechanism resulting in a weaker roll-up and thus play an important role in the wake organization.

The significance of these counter-rotating vorticity regions can be further appreciated in considering the shape factor distribution of Fig. 12(c). The counter-rotating region extends approximately to the location of the secondary peak inside the mean recirculation. The rotation opposes the reverse flow and thus acts to dampen u' fluctuations, leading to increased anisotropy ($\overline{v'^2} - \overline{u'^2} > 0$) and negative k production, as noted in Sec. IV A. While these conditions are prevalent for low-amplitude cycles, they are the contributions resulting in the negative k production and are thus statistically significant and highlight differences in the dynamics as fluctuation amplitude changes. These observations illustrate the benefit of the GPA, as the counter-rotating vorticity region is increasingly difficult to detect from the average cycle ($a_\Delta \approx 0$) as b/d increases, but does remain statistically significant.

The dynamics and structure of the wake are distinct for $b/d = 1.92$. From Fig. 16, the vortices form much further downstream (relative to x_R) than for thinner obstacles and the characteristic concentration of vorticity in the core regions is difficult to distinguish from the vorticity levels in the shear layers. The classical formation mechanism involving the roll-up of the shear layer cannot be easily identified. In contrast to the thinner cylinders, the trajectory of the centroids is independent of the a_Δ (Fig. 17), while the circulation Γ_c varies significantly (Fig. 18). As suggested by Ref. [21], the vortex formation process differs from the classical Kármán process, ostensibly due to the reattachment of the flow on the obstacle afterbody as suggested from LES simulations [31,32].

V. DISCUSSION

The rectangular-cylinder thickness can significantly impact the wake structure in terms of the Reynolds stress levels and distribution as well as the wake dynamics as exhibited by the amplitude modulation of the velocity or pressure fluctuations and the characteristics of the cycle-to-cycle variations. The variations correspond to changes in the coherent contribution to the formation region dynamics and wake structure of the vortex street. While the fluctuation amplitude and shedding phase appear to be effective observational parameters for conditional averaging, as implemented in the GPA, these are not causal, mandating further consideration with regards to underlying mechanisms. In this respect, the observation that the fluctuation amplitude is more related to the vortex trajectory than the strength of the shed vortices is of paramount importance.

The strength (i.e., Γ_c) of the shed vortices is relatively insensitive to either the changes in shedding cycle amplitude or the obstacle thickness, at least for $b/d \leqslant 1$, as seen in Fig. 18. Let Γ_o represent the average circulation delivered to the wake during a shedding cycle from the separation point, estimated from Ref. [62] to be $\Gamma_o/U_\infty d = (1 - C_{pb})/2St$, where C_{pb} is the average back-pressure coefficient. For a wide range of obstacles, including circular [57], square [12], and triangular cylinders [63], $\Gamma_c/\Gamma_o \approx 0.45$.

For the thinnest plate, using the values of $C_{pb} \approx -1.4$ [2] and St from Table II and Γ from Fig. 18(a), one obtains $\Gamma/\Gamma_o \approx 0.45$. Assuming that this ratio holds for the remainder of the present cases, then the circulation generated during the different amplitude cycles changes little. However, from Fig. 14, the shedding period increases as the amplitude level decreases. Hence, the rate at which circulation is delivered to the wake, and thus the vorticity flux, must decrease as the shedding period increases.

The vorticity flux is directly related to the curvature of the separated shear layer [64,65]. During high-amplitude cycles, the flux is greater (shorter shedding period) and thus the curvature is greater, conversely the formation length is shorter, than during low-amplitude cycles. In turn, the vortices are shed from the end of the shear layer and its curvature determines the initial trajectory of the vortices. As seen in Fig. 16 and 17, the vortices are directed increasingly towards the center of the wake ($y = 0$) as the curvature increases. These variations of the shear layer curvature, and consequently the length of the recirculation region, occur over several typical shedding periods and thus highlight the significance of representing the base flow fluctuations through the slow-varying contribution.

Since Γ_c changes little with b/d or between cycles, local increases, for example along $y = 0$, in the Reynolds stress and k levels as b/d increases from 0.05 to 1.0 must be related to both the amplitude-dependent vortex trajectory and the relative probability of occurrence, since the main contribution to $\overline{v'^2}$ and k is due to the coherent shedding motion. As the vortex centers of the opposing streets move closer during the high-amplitude cycles, the vortex-induced fluctuations along the wake center are significantly higher than for low-amplitude cycles. Since the average of squares is weighted towards higher amplitude fluctuations, the high-amplitude cycles tend to contribute more than low-amplitude cycles to k. This effect is then compounded as the low-amplitude cycles occur very rarely for $b/d = 1.0$ and very often for $b/d \lesssim 0.6$.

The foregoing results are consistent with earlier observations that the presence of the afterbody has a stabilizing effect on the separated shear layer [66]. The relative occurrence of low-amplitude cycles is related to the cycle-to-cycle variations in the separated shear layer curvature. In turn, the curvature is related to the pressure behind the separation point, which is fixed at the leading edge for sharp-edged obstacles [62]. For $b/d = 1$, the mean pressure is nearly constant over the side faces and the surface pressure fluctuations, $\overline{p'^2}$, vary little from the leading edge to approximately $0.7d$ downstream [9,13,28,32,67]. In this region, the largest contributions to $\overline{p'^2}$ are due to the periodic fluctuations. These fluctuations vary little between cycles and are uniform in phase and amplitude [13]. The above observations agree well with numerical simulations for $0.8 \leqslant b/d < 2$, which also show that the fluctuations of the lift coefficient are only weakly modulated [30,32]. On the back face $\overline{p'^2}$ is significantly lower than that on the side faces [9,13,67]. Phase-averaged velocity measurements for $b/d = 1$ [68] show that the shear layer intermittently reattaches on the side faces close to the trailing edge, thereby interrupting the communication between the separated regions over the side faces and the obstacle base.

In contrast, for thin plates the base pressure fluctuations are easily communicated to the separation point and the stabilizing effect of the afterbody is absent, resulting in a strong feedback expressed through large amplitude modulations of the wake fluctuations. Numerical simulations [30,32] show that as b/d is reduced below the critical thickness: The shear layer does not reattach on the side faces; the mean pressure distribution on the side faces is no longer uniform; $\overline{p'^2}$ increases significantly close to the leading edge; and the lift fluctuations are increasingly modulated. It thus appears that

the critical thickness and the modulation of the wake fluctuations are related to the strength of the wake feedback mechanism.

In light of the foregoing analysis and discussion, further attention is now given to the large scatter observed in the reported results for C_d and St from different earlier studies. Several studies, including Refs. [16,27,33,34,69], have shown that the flow past a rectangular sharp-edged cylinder is affected by the free-stream turbulence intensity Tu and scale, the tunnel blockage B, Re, the span-to-width aspect ratio AR, and the end conditions. For large b/d, the separated shear layer reattaches upstream of the trailing edge, so that the state of the redeveloping boundary layer is critical to the wake dynamics [21,31]. It is almost trite to state that Re and Tu will have a significant effect, since these affect both the transition and thickness of the separated shear layer or the state of the redeveloping boundary layer. In the range of parameters found in most studies, the flow development is very sensitive to these parameters. It is thus not surprising that for $b/d \sim 2$, there is a very large scatter in the reported results. Hence, attention is focused on the thinner geometries $b/d < 2$.

A comparison of the results reported by Refs. [8,9,23,27,29,34,35,70,71] suggest that for Tu $< 2\%$ the flow dynamics are relatively insensitive to the turbulence intensity. For Tu in the range 2% to 5%, they generally result in a reduction of the critical thickness. This is consistent with observations that for $b/d > 0.7$, little difference for Tu $< 5\%$ is reported. For $b/d \sim 0.6$ a decrease in C_d is typically reported while for $b/d < 0.2$ it is an increase. Increasing Tu above 6% generally leads to significant perturbation of the separated shear layer and thus the vortex formation process and significant changes in the wake dynamics are observed, which are more pronounced for the thinner obstacles [8,72]. Reference [27] notes that increasing the turbulence integral length scale to the order of the d has similar effects. These observations indicate that Tu in the range 2–5% is sufficiently large to strengthen the feedback mechanism, affecting the vorticity flux from the leading edge separation and thus reduce the critical thickness. The results for Tu $< 2\%$ are presented for C_d and St in Fig. 9. Results at Tu $= 0.06\%$ [23] and 0.6% [35] are very similar, but differ from those of Ref. [39] at Tu $= 0.12\%$ or Ref. [29] at 0.5%. Thus the scatter cannot be attributed to changes in the free-stream turbulence alone.

While it is known that an increase in the blockage will increase St and C_d, the difference observed in the results of Fig. 9 are much larger than can be accounted for with blockage corrections [73]. The blockage is generally small ($B < 5\%$) for the studies given in Table III. References [16] and [35] have corrected their data for blockage, while the remainder of the studies in Table III are reported uncorrected. The present results were conducted in an open section wind tunnel with $B \approx 3.5\%$, and thus minimal blockage effect is expected.

For $b/d < 2$, the discrepancies between results reported for C_d and St, as shown in Fig. 9, occur principally for the thin-plate regime $b/d < 0.8$. It is noted that the reported values for the critical thickness, b/d, at which the maximum C_d occurs, varies from 0.38 to 0.67. Moreover, the experimental conditions differ significantly between studies in terms of Re, AR, and whether end plates were used.

In the cylinder-like regime ($\sim 0.8 < b/d < 2$), reported values of St and C_d are insensitive to the Reynolds number, for $Re > 6\,000$—cf. Refs. [8,16,21,34]—for aspect ratios AR > 20 without the use of end plates [69] or as low as AR ~ 7 when suitable end plates are used [34]. This observation is consistent with the present results. For rectangular cylinders, the separation point is fixed at the leading corners and the afterbody is sufficiently long to suppress the wake feedback mechanism. In contrast, for the circular cylinder, where the separation point on the body is not fixed, the influence of Re, AR, and end plates is much more pronounced [74,75].

Around the critical thickness for the thin-plate regime, the obstacle is insufficiently long (i.e., thick) to suppress the feedback mechanism and an increased sensitivity to Re and AR is observed. For example, Ref. [34] reported that for a constant $Re = 90\,000$, as the aspect ratio is reduced from 20 to 6, the critical thickness decreases even with the use of end plates, as seen in Fig. 19. Reference [16] found that the pressure on the front face of rectangular cylinders is insensitive to b/d or Re. In contrast, whereas the back pressure C_{pb} (and thus C_d) for $b/d = 1.0$ was insensitive to Re, for $b/d = 0.6$, C_d changed significantly as a function of Re as shown in Fig. 20. The present

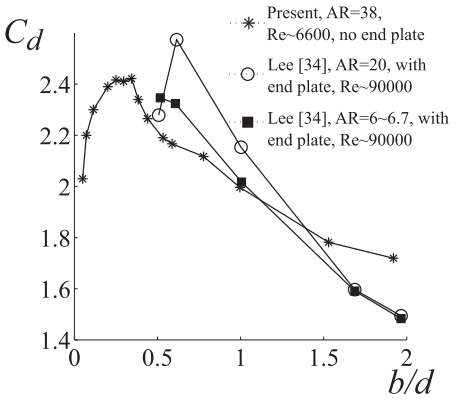

FIG. 19. Present C_d results (AR = 38, no end plates, $Re \sim 6\,600$), Ref. [34] C_d results (AR = 20, with end plates, $Re = 90\,000$), and Ref. [34] C_d results (AR = 6 to 6.7, with end plates, $Re = 90\,000$).

results are consistent with this observation. As Re is reduced, the critical thickness occurs at smaller b/d such that at a fixed $b/d = 0.6$ the drag coefficient would be observed to decrease (i.e., C_{pb} increases).

Based on the foregoing observation, an additional experiment[5] to measure the mean back pressure C_{pb} were conducted for the thinnest plate ($b/d = 0.05$). Pressure taps were placed about the centerline ($y = 0$) at $z/d = 0, \pm 4$, and ± 10, covering the range of stereo-PIV measurements. Experiments were conducted with and without end plates for $10\,000 < Re < 20\,000$. The end plates were mounted on the cylinders at the edge of the flow stream. In both cases, within the experimental uncertainty of ± 0.06, C_{pb} did not vary with z as would be expected for a mean 2D wake. Without end plates $C_{pb} \simeq -0.96 \pm 0.06$ and with end plates $C_{pb} \simeq -1.20 \pm 0.06$. Assuming that $C_p \approx C_{pb}$ over the entire back face and that the pressure distribution on the windward side of the plate does not change and is close to the stagnation pressure, the use of end plates accounts for less than 15% change in the drag coefficient and is thus less than the scatter observed from the different studies.

In contrast to the results of Ref. [16] for $b/d = 0.6$, for $b/d = 0.05$ values of C_{pb} were insensitive to Re up to 20 000, which is consistent with the earlier observation that C_d did not vary with Re in

[5]The authors would like to thank an anonymous reviewer for this suggestion.

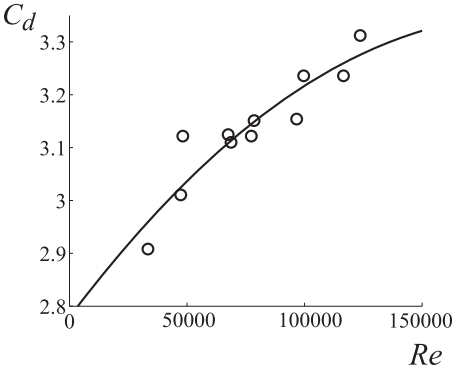

FIG. 20. C_d results deduced from $-C_{pb}$ values in Ref. [16] for the critical thickness $b/d = 0.6$ for $36\,000 < Re < 130\,000$ with a second-order polynomial fit.

this range (Fig. 6). These results suggest that the critical thickness is very sensitive to end conditions and *Re* and that changes in the critical thickness may underlie much of the scatter observed when comparing results from different studies.

VI. CONCLUSION

The results of a stereoscopic particle image velocimetry study of the nearly periodic, turbulent wakes of two-dimensional rectangular cylinders normal to a uniform flow are presented for thickness-to-chord ratios between $b/d = 0.05$ and 1.92 at a Reynolds number around 6 600. Based on a generalized phase average approach, the coherent contributions to cycle-to-cycle variations of the fluctuating velocity field are quantified. The dynamics of vortex formation and shedding are then investigated for different b/d as a function of fluctuation amplitude.

Three flow regimes can be identified based on b/d. For the thin-plate regime, the mean drag coefficient increases with b/d to a critical value: $(b/d)_c \approx 0.34$ in this study. In this regime, the wake is characterized by highly modulated fluctuation amplitudes and variations in the shedding frequency as well as intervals in which shedding activity is suppressed. This dynamic behavior can be attributed to a feedback mechanism between the formation and base regions. During low-amplitude cycles, the shedding frequency decreases significantly (i.e., the formation time increases) and coherent structures directly behind the plate corners (indicated by arrows in Fig. 16) are observed. The vorticity associated with these structures opposes that of the adjacent separated shear layer. When compared to higher amplitude cycles, the roll-up of the shear layer is delayed and the forming vortices penetrate less deeply into the base flow region. This process appears to give rise to areas of negative k production in the base region not observed for other regimes.

For larger thickness ratios, the presence of the afterbody acts to suppress the feedback mechanism between the formation and plate-base region. In the cylinder-like regime ($(b/d)_c < b/d \lesssim 1.6$), the mean drag coefficient decreases for increasing b/d and the cycle-to-cycle variations of the shedding process are much less pronounced. In this regime, intervals of suppressed vortex shedding activity are rarely observed. The long-plate regime ($b/d \gtrsim 1.6$) is characterized by reattachment of the shear layer on the afterbody. The wake dynamics differ significantly from those for smaller b/d and the wake periodicity is not associated with the classical Kármán formation and shedding process. For this regime, the state of the redeveloping boundary layer on the afterbody confers on the wake dynamics an increased sensitivity to the Reynolds number and the free-stream turbulence intensity as observed from a comparison of several studies.

The significance of the feedback mechanism for thin plates helps reconcile discrepancies when comparing trends in the Strouhal number, drag coefficient, and the critical thickness (b/d for maximum drag) for earlier studies. Similarly to circular cylinders, the communication between the wake formation region and the separation point results in a sensitivity to the Reynolds number and end conditions.

For the plate flow, this sensitivity can be observed as a change of the critical thickness and is the subject of ongoing studies. In contrast, for the cylinder-like regime (e.g., the square cylinder), these effects are suppressed due to the presence of the afterbody.

More generally, the present analysis highlights the importance of the slow-varying base-flow fluctuations on the shedding dynamics. Despite very large cycle-to-cycle variations of the fluctuating velocity amplitude and shedding period, the strength (i.e., circulation) of the shed vortices changes remarkably little for different-amplitude cycles or as a function of b/d. The instantaneous dynamics, wake topology, and fluctuation intensity are directly related to changes in the separated shear shear layer curvature and the trajectory of the shed vortices. When compared to low-amplitude cycles, the high-amplitude shedding cycles are characterized by a shorter formation length and a higher curvature of the separated shear layer. Once shed, the vortices from opposing sides move closer to the mean-flow symmetry line ($y = 0$). For low-amplitude cycles, in contrast, the trajectory of the vortices leads away from $y = 0$. During the high-amplitude cycles, larger magnitude coherent fluctuations are induced due to the relative proximity of the shed vortices and, conversely, lower magnitude

coherent fluctuations during low-amplitude cycles. Hence, resolving the vortex topology—in this case, particularly, the cycle-to-cycle variation in the vorticity distribution and relative location of the vortex cores—is important for interpreting the fluctuation dynamics. The aforementioned behavior illustrates mechanisms consistent with energetic exchanges between the slow-varying motion associated with the base flow and the oscillatory motion due to vortex shedding as described in mean-field theory.

ACKNOWLEDGMENTS

This work was supported by the NSERC Industrial Research Chairs program and the ENMAX Corporation, and the NSERC Discovery Scheme.

---

[1] T. Igarashi, Fluid flow and heat transfer around rectangular cylinders (the case of a width/height ratio of a section of 0.33 to 1.5), Int. J. Heat Mass Transf. **30**, 893 (1987).
[2] A. Fage and F. C. Johansen, On the flow of air behind an inclined flat plate of infinite span, Proc. R. Soc. London, Ser. A **116**, 170 (1927).
[3] M. Arie and H. Rouse, Experiments on two-dimensional flow over a normal wall, J. Fluid Mech. **1**, 129 (1956).
[4] F. H. Abernathy, Flow over an inclined plate, J. Basic Eng. **84**, 380 (1962).
[5] L. J. S. Bradbury, Measurements with a pulsed-wire and a hot-wire anemometer in the highly turbulent wake of a normal flat plate, J. Fluid Mech. **77**, 473 (1976).
[6] A. Leder, Dynamics of fluid mixing in separated flows, Phys. Fluids A **3**, 1741 (1991).
[7] D. L. A. Lisoski, Nominally 2-dimensional flow about a normal flat plate, Ph.D. thesis, California Institute of Technology, Pasadena, 1993 (unpublished).
[8] B. J. Vickery, Fluctuating lift and drag on a long cylinder of square cross-section in a smooth and in a turbulent stream, J. Fluid Mech. **25**, 481 (1966).
[9] B. E. Lee, The effect of turbulence on the surface pressure field of a square prism, J. Fluid Mech. **69**, 263 (1975).
[10] D. O. Rockwell, Organized fluctuations due to flow past a square cross section cylinder, J. Fluids Eng. **99**, 511 (1977).
[11] E. D. Obasaju, An investigation of the effects of incidence on the flow around a square section cylinder, Aeronaut. Quarterly **34**, 243 (1983).
[12] D. A. Lyn, S. Einav, W. Rodi, and J. H. Park, A laser-doppler velocimetry study of ensemble-averaged characteristics of the turbulent near wake of a square cylinder, J. Fluid Mech. **304**, 285 (1995).
[13] S. C. C. Bailey, G. A. Kopp, and R. J. Martinuzzi, Vortex shedding from a square cylinder near a wall, J. Turbulence **3**, N3 (2002).
[14] H. Nakaguchi, K. Hashimoto, and S. Muto, An experimental study on aerodynamic drag of rectangular cylinders, J. Jpn. Soc. Aeronaut. Space Sci. **168**, 1 (1968).
[15] G. V. Parkinson and D. Dicker, Wind-induced instability of structures, Philos. Trans. R. Soc. London, Ser. A **269**, 395 (1971).
[16] P. W. Bearman and D. M. Trueman, An investigation of flow around rectangular cylinders, Aeronaut. Quarterly **23**, 229 (1972).
[17] J. Novak, Strouhal number of a quadrangular prism, angle iron, and two circular cylinders arranged in tandem, Acta Techn. CSAV **20**, 366 (1974).
[18] K. Washizu, A. Ohya, Y. Otsuki, and K. Fujii, Aeroelastic instability of rectangular cylinders in a heaving mode, J. Sound Vib. **59**, 195 (1978).
[19] A. Laneville and C. D. Williams, The effect of intensity and large scale turbulence on the mean pressure and drag coefficients of 2d rectangular cylinders, in *Proceedings of the 5th International Conference on Wind Effects on Building and Structures*, edited by J. E. Cermak (Pergamon Press, Oxford, 1980).

[20] A. Ohya, K. Washizu, K. Fujii, and Y. Otsuki, Wind tunnel experiments on aerodynamic forces and pressure distributions of rectangular cylinders in a uniform flow (part 2), in *Proceedings 6th National Symposium on Wind Engineering (Japan)* (Tokyo, 1980), pp. 153–160.
[21] A. Okajima, Strouhal numbers of rectangular cylinders, J. Fluid Mech. **123**, 379 (1982).
[22] T. Igarashi, Characteristics of the flow around rectangular cylinders: The case of the angle of attack 0 deg, Bull. JSME **28**, 1690 (1985).
[23] C. Norberg, Flow around rectangular cylinders: Pressure forces and wake frequencies, J. Wind Eng. Indust. Aerodyn. **49**, 187 (1993).
[24] Y. Nakamura and K. Hirata, Critical geometry of oscillating bluff bodies, J. Fluid Mech. **208**, 375 (1989).
[25] M. Matsumoto, H. Ishizaki, C. Matsuoka, Y. Daito, Y. Ichikawa, and A. Shimahara, Aerodynamic effects of the angle of attack on a rectangular prism, J. Wind Eng. Indust. Aerodyn. **77**, 531 (1998).
[26] M. Matsumoto, Vortex shedding of bluff bodies: A review, J. Fluids Structures **13**, 791 (1999).
[27] Y. Nakamura and Y. Ohya, The effects of turbulence on the mean flow past two-dimensional rectangular cylinders, J. Fluid Mech. **149**, 255 (1984).
[28] Y. Ohya, Note on a discontinuous change in wake pattern for a rectangular cylinder, J. Fluids Struct. **8**, 325 (1994).
[29] C. W. Knisely, Strouhal numbers of rectangular cylinders at incidence: A review and new data, J. Fluids Struct. **4**, 371 (1990).
[30] T. Tamura and Y. Itoh, Unstable aerodynamic phenomena of a rectangular cylinder with critical section, J. Wind Eng. Indust. Aerodyn. **83**, 121 (1999).
[31] A. Sohankar, Large eddy simulation of flow past rectangular-sections cylinders: Side ratio effects, J. Wind Eng. Indust. Aerodyn. **96**, 640 (2008).
[32] D. Yu, K. Butler, A. Kareem, J. Glimm, and J. Sun, Simulation of the influence of aspect ratio on the aerodynamics of rectangular prisms, J. Eng. Mech. **139**, 429 (2013).
[33] B. E. Lee, The susceptibility of tests on two-dimensional bluff bodies to incident flow variations, J. Wind Eng. Indust. Aerodyn. **2**, 133 (1977).
[34] B. E. Lee, Some observations of the effect of aspect ratio on the influence of turbulence on the drag of rectangular cylinders, J. Wind Eng. Indust. Aerodyn. **33**, 107 (1990).
[35] J. Courchesne and A. Laneville, A comparison of correction methods used in the evaluation of drag coefficient measurements for two-dimensional rectangular cylinders, J. Fluids Eng. **101**, 506 (1979).
[36] F. M. Najjar and S. Balachandar, Low-frequency unsteadiness in the wake of a normal flat plate, J. Fluid Mech. **370**, 101 (1998).
[37] S. J. Wu, J. J. Miau, C. C. Hu, and J. H. Chou, On low-frequency modulations and three-dimensionality in vortex shedding behind a normal plate, J. Fluid Mech. **526**, 117 (2005).
[38] Y. Otsuki, K. Washizu, H. Tomizawa, and A. Ohya, A note on the aeroelastic instability of a prismatic bar with square section, J. Sound Vib. **34**, 233 (1974).
[39] Y. Ohya, Y. Nakamura, S. Ozono, H. Tsuruta, and R. Nakayama, A numerical study of vortex shedding from flat plates with square leading and trailing edges, J. Fluid Mech. **236**, 445 (1992).
[40] J. A. Bourgeois, B. R. Noack, and R. J. Martinuzzi, Generalized phase average with applications to sensor-based flow estimation of the wall-mounted square cylinder wake, J. Fluid Mech. **736**, 316 (2013).
[41] J. T. Stuart, On the non-linear mechanics of hydrodynamic stability, J. Fluid Mech. **4**, 1 (1958).
[42] M. P. Arroyo and C. A. Greated, Stereoscopic particle image velocimetry, Meas. Sci. Technol. **2**, 1181 (1991).
[43] S. K. Sinha and P. S. Kuhlman, Investigating the use of stereoscopic particle streak velocimetry for estimating the three-dimensional vorticity field, Exp. Fluids **12**, 377 (1992).
[44] A. K. Prasad and R. J. Adrian, Stereoscopic particle image velocimetry applied to liquid flows, Exp. Fluids **15**, 49 (1993).
[45] A. K. Prasad, Steresocopic particle image velocimetry, Exp. Fluids **29**, 103 (2000).
[46] S. M. Soloff, R. J. Adrian, and Z. C. Liu, Distortion compensation for generalized stereoscopic particle image velocimetry, Meas. Sci. Technol. **8**, 1441 (1997).

[47] M. Raffel, C. E. Willert, S. Wereley, and J. Kompenhans, *Particle Image Velocimetry: A Practical Guide* (Springer, Berlin, 2013).
[48] A. J. Wheeler and A. R. Ganji, *Introduction to Engineering Experimentation*, 3rd ed. (Prentice Hall, Englewood Cliffs, NJ, 2009).
[49] A. K. M. F. Hussain and W. C. Reynolds, The mechanics of an organized wave in turbulent shear flow, J. Fluid Mech. **41**, 241 (1970).
[50] R. Perrin, M. Braza, E. Cid, S. Cazin, A. Barthet, A. Servain, C. Mockett, and F. Thiele, Obtaining phase averaged turbulence properties in the near wake of a circular cylinder at high reynolds number using pod, Exp. Fluids **43**, 341 (2007).
[51] P. Holmes, J. L. Lumley, G. Berkooz, and C. W. Rowley, *Turbulence, Coherent Structures, Dynamical Systems, and Symmetry* (Cambridge University Press, Cambridge, UK, 2012).
[52] B. R. Noack, K. Afanasiev, M. Morzynski, G. Tadmor, and F. Thiele, A hierarchy of low-dimensional models for the transient and post-transient cylinder wake, J. Fluid Mech. **497**, 335 (2003).
[53] Z. Hosseini, R. J. Martinuzzi, and B. R. Noack, Sensor-based estimation of the velocity in the wake of a low-aspect-ratio pyramid, Exp. Fluids **56**, 13 (2015).
[54] Z. Hosseini, R. J. Martinuzzi, and B. R. Noack, Modal energy analysis of a highly modulated wake behind a wall-mounted pyramid, J. Fluid Mech. **798**, 717 (2016).
[55] R. A. Antonia and S. Rajagopalan, Determination of drag of a circular cylinder, AIAA J. **28**, 1833 (1990).
[56] Y. Zhou, M. d. Mahbub Alam, H. X. Yang, H. Guo, and D. H. Wood, Fluid force on a very low Reynolds number airfoil and their prediction, Int. J. Heat **32**, 329 (2011).
[57] B. Cantwell and D. Coles, An experimental study of entrainment and transport in the turbulent near wake of a circular cylinder, J. Fluid Mech. **136**, 321 (1983).
[58] M. E. Davies, A comparison of the wake structure of a stationary and oscillating bluff body, using a conditional averaging technique, J. Fluid Mech. **75**, 209 (1976).
[59] J. F. Claerbout, *Fundamentals of Geophysical Data Processing* (McGraw-Hill, New York, 1976).
[60] J. H. Gerrard, Mechanics of the formation region of vortices behind bluff bodies, J. Fluid Mech. **25**, 401 (1966).
[61] B. Alhorn, M. Lefrancois, and D. H. King, The clockwork of vortex shedding, Phys. Essays. **11**, 144 (1998).
[62] A. Roshko, A new hodograph for free-streamline theory, National Advisory Committee for Aeronautics Technical Note 3168, Washington, 1954 (unpublished).
[63] A. L. Csiba and R. J. Martinuzzi, Investigation of bluff body asymmetry on properties of vortex shedding, J. Wind Eng. Indust. Aerodyn. **96**, 1152 (2008).
[64] C. H. K. Williamson and A. Roshko, Measurements of base pressure in the wake of a cylinder at low Reynolds numbers, Zeitsch. Flugwissensch. Weltraumforsch. **14**, 38 (1990).
[65] A. Roshko, Perspectives on bluff body aerodynamics, J. Wind Eng. Indust. Aerodyn. **49**, 79 (1993).
[66] S. Balachandar, R. Mittal, and F. M. Najjar, Properties of the mean recirculation region in the wakes of two-dimensional bluff bodies, J. Fluid Mech. **351**, 167 (1997).
[67] P. W. Bearman and E. D. Obasaju, An experimental study of pressure fluctuations on fixed and oscillating square-section cylinders, J. Fluid Mech. **119**, 297 (1982).
[68] D. A. Lyn and W. Rodi, The flapping shear layer formed by flow separation from the forward corner of a square cylinder, J. Fluid Mech. **267**, 353 (1994).
[69] E. D. Obasaju, On the effects of end plates on the mean forces on square sectioned cylinders, J. Wind Eng. Indust. Aerodyn. **5**, 179 (1979).
[70] A. Laneville, I. S. Gartshore, and G. V. Parkinson, An explanation of some effects of turbulence on bluff bodies, in *Proceedings 4th International Conference on Wind Effects on Buildings and Structures, Heathrow, England*, edited by K. J. Eaton (Cambridge University Press, Cambridge, UK, 1975), p. 333.
[71] J. Courchesne and A. Laneville, An experimental evaluation of drag coefficient for rectangular cylinders exposed to grid turbulence, ASME J. Fluids Eng. **104**, 523 (1982).
[72] J. Novak, Strouhal number and flat plate oscillation in an air stream, Acta Tech. Csav. **18**, 372 (1973).
[73] J. B. Barlow, W. H. Rae, and A. Pope, *Low-Speed Wind Tunnel Testing*, 3rd ed. (John Wiley and Sons, New York, 1999), p. 355.

[74] M. Gharib and A. Roshko, The effect of flow oscillations on cavity drag, J. Fluid Mech. **177**, 501 (1987).

[75] M. Hammache and M. Gharib, An experimental study of the parallel and oblique vortex shedding from circular cylinders, J. Fluid Mech. **232**, 567 (1991).